INSTITUTO SUPERIOR DE ENGENHARIA DO PORTO
MESTRADO EM ENERGIAS SUSTENTÁVEIS

Caracterização avançada de células fotovoltaicas de filme fino tipo CIGS

PEDRO DUARTE ALVES MONTEIRO
novembro de 2023

POLITÉCNICO
DO PORTO

INSTITUTO SUPERIOR DE ENGENHARIA DO PORTO

DISSERTAÇÃO
MESTRADO EM ENERGIAS SUSTENTÁVEIS

Advanced characterization of CIGS thin-film photovoltaic cells

Pedro Duarte Alves Monteiro

POLITÉCNICO DO PORTO

September 2023

INSTITUTO SUPERIOR DE ENGENHARIA DO PORTO

DISSERTAÇÃO
MESTRADO EM ENERGIAS SUSTENTÁVEIS (MES)

Advanced characterization of CIGS thin-film photovoltaic cells

Nome do autor: Pedro Duarte Alves Monteiro

Número de estudante: 1210148

Dissertação apresentada ao Instituto Superior de Engenharia do Porto para cumprimento dos requisitos necessários à obtenção do grau de Mestre em Energias Sustentáveis.

Orientador:

Prof. Dr. Paulo Fernandes

Co-orientador:

Dr. Jennifer Teixeira

26 setembro 2023

ABSTRACT

Keywords

Efficiency, CIGS, oxidation, photovoltaic energy, thin-film

The world is currently facing a global energy crisis which requires investment in new energy production technologies. Renewable energy sources are becoming increasingly important as an alternative and complement to fossil energy sources. A highlight in this scenario is solar energy, especially photovoltaic production, since it can be used in a variety of environments and scales. The use of solar energy has evolved over the years, with new structures and materials being sought for their development, one such solution being second-generation solar cells based on copper, indium, gallium and selenium, known as CIGS. However, mass production of these cells faces challenges such as oxidation and lack of sodium, which are difficult to overcome. To understand how these problems affect solar cells, a study based on electrical tests were carried out, including measurements of current vs voltage, external quantum efficiency, capacitance vs voltage, light intensity-dependent current vs voltage and temperature-dependent current vs voltage. The results show that both production problems have a negative impact on solar cells, with oxidation causing only a small reduction in efficiency, while a lack of sodium leads to the creation of electron barriers and high recombination rates, resulting in a significant loss of efficiency.

RESUMO

Palavras Chave

Eficiência, CIGS, energia fotovoltaica, filmes finos, oxidação

O mundo enfrenta atualmente uma crise energética global existindo a necessidade de investimento em novas tecnologias para produção de energia. As fontes de energia renovável estão a tornar-se cada vez mais importantes como alternativa e complemento às fontes de energia fóssil. Um destaque nesse cenário é a energia solar, especialmente a produção fotovoltaica, uma vez que pode ser usada numa grande variedade de ambientes e escalas. O aproveitamento da energia solar tem evoluído ao longo dos anos, procurando-se novas estruturas e materiais para o desenvolvimento das mesmas, sendo uma dessas soluções as células solares de segunda geração baseadas em Cobre, Índio, Gálio e Selénio, conhecidas como CIGS. No entanto, a produção massificada destas células enfrenta desafios, como oxidação e falta de sódio, que são difíceis de eliminar. Para entender como esses problemas afetam as células solares, foi realizado um estudo baseado em medidas elétricas, incluindo medições de corrente vs tensão, eficiência quântica externa, capacitância vs tensão, corrente vs tensão dependente da intensidade de luz e corrente vs tensão dependente de temperatura. Os resultados mostram que ambos os problemas de produção têm um impacto negativo nas células solares, sendo que a oxidação causa apenas uma pequena redução na eficiência, enquanto a falta de sódio leva a criação de barreiras de eletrões e altas taxas de recombinação, resultando em uma perda significativa de eficiência.

ACKNOWLEDGMENTS

First of all, I would like to express my deepest gratitude to my family, who have been a fundamental pillar throughout my journey as a student. Without their tireless support, the path I have travelled would not have been possible. I thank them from the bottom of my heart for always being by my side.

I would also like to extend my thanks to the INL - International Iberian Nanotechnology Laboratory, which granted me access to all its facilities. My thanks go to the remarkable team of NOA, who made the months I spent there truly memorable. Working with them on a day-to-day basis was an enriching experience that contributed immensely to my professional and personal growth. I would like to express special thanks to my tutors, Prof. Dr. Paulo Fernandes and Dr. Jennifer Teixeira, for the time they invested in me and for their infinite patience. To PhD student Marco Alberto, who often put his own PhD thesis on the back burner to help me in times of need, I am deeply grateful.

Last but not least, I would like to extend my gratitude to all my friends who listened to my problems and supported me through the difficult times with smiles on their faces. I would also like to thank my three fellow interns, António Monteiro, Enzo Ribeiro and Pedro Rebola, who have been my conversation partners over the last seven months and have helped to make this journey even more meaningful.

I am truly blessed to have had such incredible people in my life, and this achievement is as much yours as it is mine. Thank you all for your constant support and for the fundamental role you have played in my trajectory.

Pedro Monteiro

“When you die, you can't see sunsets.”

Hayao Miyazaki

COVERALL INDEX

ABSTRACT ..... *i*

RESUMO ..... *iii*

ACKNOWLEDGMENTS ..... *v*

INDEX OF FIGURES ..... *xi*

INDEX OF TABLES ..... *xiii*

ABBREVIATIONS LIST ..... *xv*

SYMBOL LIST ..... *xvii*

CHAPTER 1 ..... *1*

1 - Introduction *1*

1.1 - PV framework **3**
1.1.1 - How a solar cell works 3
1.1.2 - First Generation - Crystalline silicon PV 4
1.1.3 - Second Generation - Thin-film PV 5
1.1.4 - Third Generation - Emerging PV 5

1.2 - Dissertation Objectives **7**

1.3 - Dissertation Structure **8**

CHAPTER 2 ..... *9*

2 - Bibliographic Review *9*

2.1 - CIGS Framework **9**
2.1.1 - Layers 10

CHAPTER 3 ..... *16*

3 - Processes and methodology *16*

3.1 - Devices characterization **16**
3.1.1 - Reference device 18
3.1.2 - O_2 device 18
3.1.3 - Sodium free device 18

3.2 - Current density vs voltage **18**
3.2.1 - Experimental data 22

3.3 - Ideality factor **27**
3.3.1 - Experimental data 28

3.4 - Quantum efficiency **30**
3.4.1 - Experimental data 31

3.5 - Capacitance vs Voltage **33**
3.5.1 - Mott-Schottky Plot 34
3.5.2 - Derivative method 35

3.6 - Light intensity dependent current density vs voltage **38**
3.6.1 - Experimental data 40

3.7 - Temperature dependent current density vs voltage **42**
3.7.1 - Experimental data 44

CHAPTER 4 46
4 - Results and discussion 46
CHAPTER 5 51
5 - Conclusions and future work 51
5.1 - Conclusions 51
5.2 - Future work 52
BIBLIOGRAPHICAL REFERENCES 53
ANNEXES 60
ANNEX A – EXPERIMENTAL RESULTS 60

INDEX OF FIGURES

Figure 1 - Variation in the production of the various types of energy sources in the first semester of 2022, extracted from (Wiatros-Motyka et al., 2022) 2

Figure 2 - Relation between energy needs and energy production in the first eight months of 2022, extracted from (Wiatros-Motyka et al., 2022) 2

Figure 3 - Solar cells working process, extracted from (Archer & Green, 2014) 4

Figure 4 - $Cu(In,Ga)Se_2$ crystal structure, extracted from (Durgalakshmi et al., 2020) 9

Figure 5 - Layer arrangement of a CIGS solar cell, adapted from (Salhi, 2022) 10

Figure 6 - Graphical comparison between the three co-evaporation processes, adapted from (Huang et al., 2018) 13

Figure 7 - The 3 devices and their cells, photo taken in the laboratory 17

Figure 8 - Studied devices scheme with 32 individual solar cells enumerated 17

Figure 9 - SEM cross-sectional image of a representative solar cell from the Reference device 18

Figure 10 - Characteristic JV curve of a solar cell 19

Figure 11 - Schematic illustrating the relationship between the JV curve and the parallel resistance (R_{sh}) and series resistance (R_s) 19

Figure 12 - JV setup and positioning of positive and negative contacts in the cell, photo taken in the laboratory 22

Figure 13 - Configuration of the IV_Measure.exe software and presentation of the variables used to perform the JV measurements 22

Figure 14 - Characterization of the problems and behaviours of the reference device **X**- cell with high R_S and/or low R_P **X**- cell with no photovoltaic behaviour (damaged) 23

Figure 15 - Representative JV curve and electrical values of the reference device . 24

Figure 16 - Characterization of the problems and behaviours of the O_2 device **X**- cell with high R_S and/or low R_P **X**- cell with no photovoltaic behaviour (damaged) **O**- cell characterized by cross-over behaviour 25

Figure 17 - Representative illuminate and dark JV curves and electrical values for a O_2 solar cell 25

Figure 18 - Characterization of the problems and behaviours of the Na free device **X**- cell with high R_S and/or low R_P **X**- cell with no photovoltaic behaviour (damaged) **O**- cell characterized by cross-over and roll-over behaviour at the same time 26

Figure 19 - Representative electrical values and JV curve of the Na free device showing simultaneous cross-over and roll-over behaviour 27

Figure 20 - dJ/dV vs V plot showing average values and standard deviations of the shunt conductance of each device a) reference device b) O_2 device c) Na free device 29

Figure 21 - Representative EQE spectrum for each studied device 31

Figure 22 - Representative Derivative Graph of the EQE curve of a reference device/ E (eV) = 1239.8 / λ (nm) 32

Figure 23 - Illustration of the depletion zone and its kink effect shown in an energy band diagram 33

Figure 24 - Mott-Schottky Plot and obtention of V_{bi} through linear regression 34

Figure 25 - Plot of the net concentration of acceptors vs. distance from the interface for the cells of the reference device a) cells: #2, #3, #10, #12 b) cells: #14, #15, #16, #19, #20, #21, #22, #23 36

Figure 26 - Plot of the net concentration of acceptors vs. distance from the interface for the cells of the O_2 device a) cell #2 b) representative pattern of all cells that do not show cross-over, cells: #10, #11, #12, #13, #18, #19, #20, #21, #22, #23 c) cross-over cells pattern, cell: #7, #8, #15, #24 37

Figure 27 - Plot of the net concentration of acceptors vs. distance from the interface for the cells of the Na free device a) cells: #19, #20, #21, #27, #28, #29 b) cells: #11, #13, #14, #22, #23, #30, #31 c) cell #8 38

Figure 28 - Layout of the setup used for JV filter measurements a) vertical schematic of the setup showing measurements and angles used to assemble it b) picture of the setup 40

Figure 29 - Open circuit voltage vs light intensity plot a) reference cell #19 b) cell #8 exposed to O_2, shows cross-over c) Na free cell #20 d) cell #18 exposed to O_2, normal JV behaviour 41

Figure 30 - Relation between short-circuit current and light intensity of cell #18 of the O_2 device based on linear regression 42

Figure 31 - Procedure for placing the cell in the cooling equipment to carry out JVT measurements a) open chamber, placing the cell and connecting the electrical contacts b) closed chamber, necessary condition to start the purging process 44

Figure 32 - Open circuit voltage vs temperature plot a) reference cell #19 b) Na free cell #20 c) cell #8 exposed to O_2 45

INDEX OF TABLES

Table 1 - Transmittance of light filters 39

Table 2 - Results obtained through JV measurements, averages and standard deviations 46

Table 3 - Average and standard deviation of the absorber layer bandgap energy values of the different solar cells 47

Table 4 - Average and standard deviation of the built-in voltage of different devices 48

Table 5 - Net acceptor concentration and depletion region width values, obtained through C-V tests, when V=0 48

Table 6 - Summary of the results obtained during the study that were used to obtain the recombination coefficients 50

ABBREVIATIONS LIST

Cu - Cobre

CV - Capacitance vs voltage

DC – Direct current

EQE – External quantum efficiency

Ga - Gallium

In - Indium

IQE – Internal quantum efficiency

JV – Current density vs voltage

JVT – Temperature dependent current voltage

Na - Sodium

O_2 – Oxygen

PV – Photovoltaic

QE – Quantum efficiency

Se – Selenium

SEM - Scanning electron microscope

SYMBOL LIST

a – Area (m^2)

A – Ideality factor

Ea – Recombination activation energy (eV)

Eg – Absorber bandgap (eV)

FF – Fill factor (%)

G – Shunt conductance ($mS*cm^{-2}$)

G_a – Sun intensity ($Suns^{-1}$)

J_0 - Dark saturation current (A)

J_l – Photocurrent (A)

J_{MP} - Current at maximum power point (A)

J_{SC} – Short circuit current density (A)

K - Boltzmann constant ($J*K^{-1}$)

M_P – Maximum power point (W)

N_{CV} – Net acceptors concentration ($N*cm^{-3}$)

pf – Photon flux ($photons*cm^{-2}*s^{-1}$)

P_{in} - Total incident energy (W)

R_P – Parallel resistance (Ω)

R_S – Series resistance (Ω)

R^b - Recombination coefficient at depletion region ($cm^{-2}*s^{-1}$)

R^d - Recombination coefficient at the interface ($cm^{-2}*s^{-1}$)

R^i - Sum of the interface recombination coefficients buffer/absorber and absorber/back contact ($cm^{-2}*s^{-1}$)

$R^{i,f}$ - Recombination coefficient at buffer/absorber interface ($cm^{-2}*s^{-1}$)

$R^{i,b}$ - Recombination coefficient at absorber/back contact interface ($cm^{-2}*s^{-1}$)

V_{bi} – Built-in voltage (eV)

V_{MP} - Voltage at maximum power point (V)

V_{OC} - Open circuit voltage (V)

W – Absorber thickness (m)

ξb - Bulk Fermi level above valance (Ev)
φb_0 - Hole potential barrier (eV)
λ – Wavelength (nm)
η - Efficiency (%)

CHAPTER 1

1 - Introduction

The exponential increase of human population, accompanied by technological evolution, has raised several problems, with one of them being the continuous energy demand (Sampaio & González, 2017).

Each person in the world can be represented by the amount of energy spent to meet their needs, which are not limited to the electricity spent by each person every day, but the sum of all consumption, such as the energy expenditure involved in processing food, clothing, housing, and transportation. It should also be noted that energy production cannot be limited to meet the minimum needs of the user, since as mentioned in (González-Eguino, 2015) energy availability is intrinsically linked to development.

To enable technological development, there is then the need for growth in energy production. However, this growth must be controlled, since conventional energy generation techniques, where fossil fuels are burned, have harmful effects on the environment, such as climate change, air pollution, acid rain, and others (Kumari et al., 2022). As a response to these type of side effects, the production of energy through renewable and less harmful sources has been developed through both in device improvement as in the increase in production and availability of the same in the market.

Figure 1 shows an increase in renewable energy in the first half of 2022, while coal and gas based production decreased, although the latter shows a negligible difference. This increase in renewable energy production can be translated into an increase of 416 TWh over the previous year, a higher value than the increase in electricity needs, 389 TWh. This increase resulted in a 2% increase in the market occupancy of renewable energies, and they are now able to satisfy 28% of the world's energy needs. (Wiatros-Motyka et al., 2022).

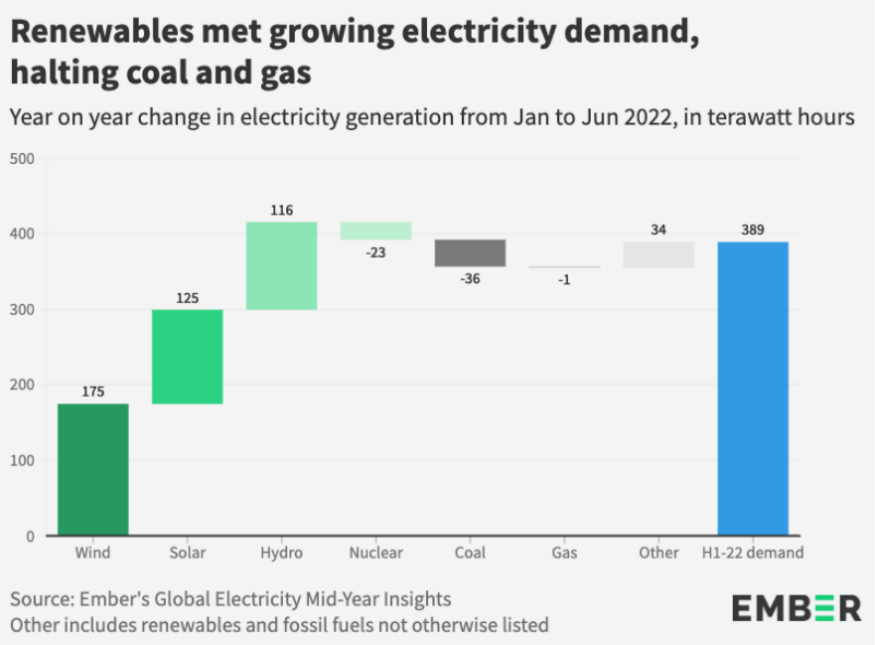

Figure 1 - Variation in the production of the various types of energy sources in the first semester of 2022, extracted from (Wiatros-Motyka et al., 2022)

Although this increase is important, it is not enough since renewable production is very volatile depending on environmental factors and seasonal variations. It can be seen in Figure 2 that in times of greater energy need this type of energy cannot respond, making it necessary to increase energy production through fossil sources.

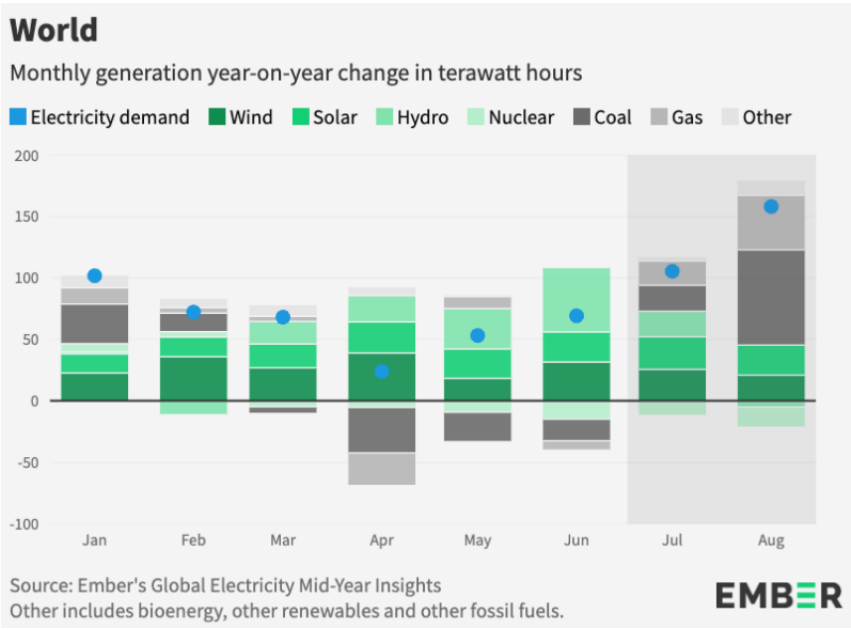

Figure 2 - Relation between energy needs and energy production in the first eight months of 2022, extracted from (Wiatros-Motyka et al., 2022)

To solve this problem, there are two solutions: the dissemination of renewable energy production sources in the grid system, which is already in progress, and improving the efficiency of PV technology so that a smaller number of devices can produce a greater amount of energy.

1.1 - PV framework

PV can be roughly defined as just converting energy from the sun into electrical energy. The fact that this type of energy does not use any type of fossil source allows it to contribute to the mitigation of negative environmental factors related to non-renewable production. According to (Peng et al., 2013), when compared to a traditional fossil-based power plant, PV technology besides mitigating greenhouse gas (GHG) emissions, can also eliminate up to 1000 tons of CO_2, 10 t of SO_2, 4 t of NO_x, and 0.7 t of particulates for each GW/h produced. However, despite the conversion process being clean, when we evaluate the life cycle of PV panels it is possible to perceive some environmental harm, from their production and assembly phase to their disposal and recycling, and in all these processes high energy costs and GHG emissions are involved, so PV production is constantly developing in order to eliminate all kinds of pollution involved.

1.1.1 - How a solar cell works

Although the basic operation of a PV panel is represented by the conversion of energy from the Sun into electrical energy, this process is more elaborate than that, since to generate energy, a voltage as well as a current must be generated. The voltage is generated in a solar cell by a process known as the PV effect (Lin & Ravindra, 2020).

The conversion process takes place after the light hits the solar cell, and not all the incident light is converted in electron-hole pairs due to optical losses caused by reflection and parasitic absorption.

In the case of $Cu(In,Ga)Se_2$ (CIGS) solar cells, a heterojunction based technology, each solar cell consists of a thin layer of n-type material and a thicker layer of p-type material (Sze & Lee, 2012). Near the junction between these layers, the electrons then start to move in order to fill the holes in the p-type layer, creating an area around the junction called the depletion zone, where electron-hole pairs are created until all the holes are filled. When incident light generates carriers and is absorbed, there is a simultaneous increase in the number of electrons in the n-type material and the number of holes in the p-type material. These electrons then start

to move in order to fill the holes, Figure 3, this flow of electrons generates an electric current.

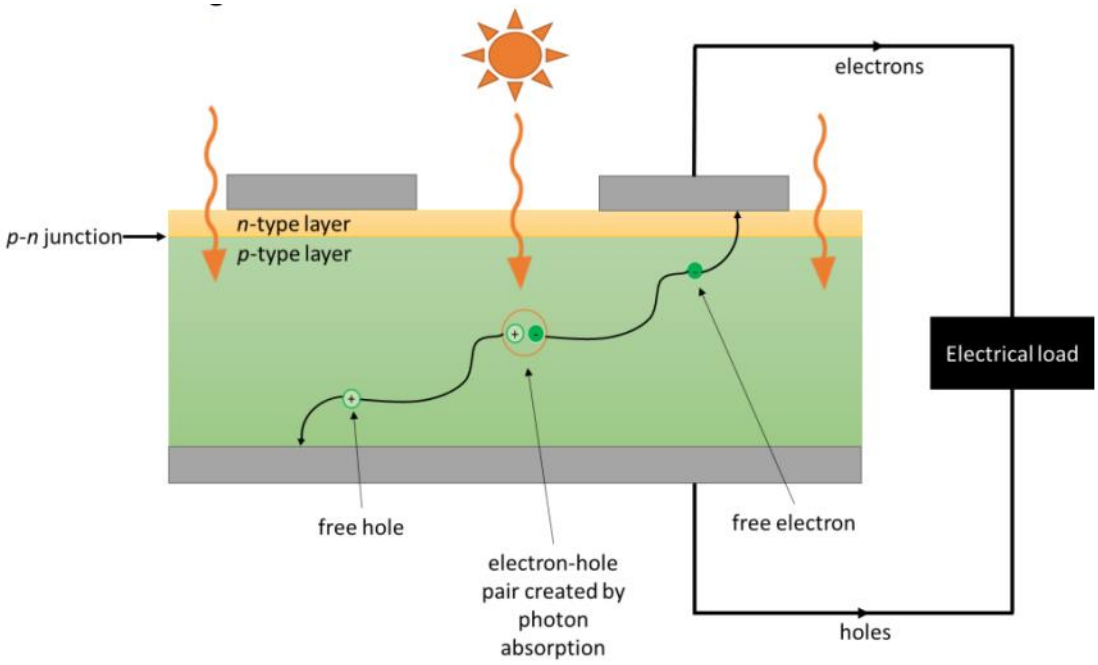

Figure 3 - Solar cells working process, extracted from *(Archer & Green, 2014)*

Although the operation of solar cells is based on the PV effect, the architecture of this type of system is not always similar, so its variations derive from the use of different materials in the various layers of the cell. Due to this kind of reorganization in the structure, photovoltaic production has been divided into 3 categories, called generations, their names being "crystalline silicon PV", "Thin-film PV" and "Emerging PV", respectively.

1.1.2 - First Generation - Crystalline silicon PV

Crystalline silicon (c-Si) as absorber layer's semiconductor material, was the first approach to implement a full functional and commercial energy conversion device (Chapin & Fuller, 2004), still being the predominant technology in the PV energy market (Kumari et al., 2022).

The wafer based Si solar cells can be divided into two categories, polycrystalline and c-Si absorber. The former undergoes less demanding production processes, resulting in a product with low efficiency, but cheap and fast production, which makes it compete with c-Si that despite presenting a slower and more expensive process manages to offer better efficiencies making it dominate the market with 84% share within the silica-based production (Kumari et al., 2022).

Within the advanced silicon, it is worth mentioning the PERC (passivated emitter rear cell) technologies, which differ by the use of an aluminum oxide deposition, which is used for passivation and allows this type of cell to have a maximum confirmed efficiency of 24.5% (Enkhardt, 2022), and the HJT technology (Heterojunction cell) that counts on an intrinsic thin film and has the record efficiency, among all first generation technologies, of 26.81% (Jacobo, 2022).

1.1.3 - Second Generation - Thin-film PV

The thin-film, as the name indicates, is characterized by its thin absorber layer if compared to the first generation, this being possible due to the fact that this technology absorber has a direct bandgap, which means an increase in the absorption coefficient, allowing the reduction of the absorber material, which in itself already presents a great advantage since it allows the creation of lighter devices, as well as the possibility of reducing production costs (Parida et al., 2011). This second generation can be further divided into two other categories:

Silicon-based PV thin film where one finds amorphous silicon (a-Si) panels that have as their only advantage their low cost, being left behind since they never exceeded 10.09% efficiency dyed in 2009 (Meier et al., 2009).

There are also those not based on silicon, where we find the CdTe technology, with the largest market share within the second generation, showing a maximum efficiency of 22.1% (Scully, 2021), but with the disadvantage that cadmium is toxic and tellurium is relatively rare (Khan et al., 2022; Z. Li et al., 2022); and its competitor in performance CIGS, with a maximum efficiency of 23.35% (Nakamura et al., 2019a), but which has not asserted itself in the market because the acquisition of Indium has a high cost due to its scarcity.

1.1.4 - Third Generation - Emerging PV

Third generation PV aims to create technology with high efficiency and low prices, while use thin films (Conibeer, 2007). It should be noted, however, that this type of devices is still largely in the development stage.

It has dye-sensitized PV, organic PV and perovskite PV as its main references, these being in increasing order of maximum efficiency. The disadvantage of dye-sensitized is its sensitivity to temperature variation,

which affects the functioning of the cell, although it manages to have an affordable price and an efficiency of 13% (Photovoltaics report, 2022), the lower. Organic PV is based on the strict use of organic materials or polymers (Kumari et al., 2022), despite its low cost, flexibility, lightness and no presence of toxic elements, the fact that it has poor environmentally resistant structure and an efficiency of 19% (Chen et al., 2023). Finally, as the most competitive with an efficiency of 25.7% (Green et al., 2022), and that like the previous ones can be produced at low cost, has the disadvantage of its rapid degradation and the presence of a toxic metal in its composition, lead (Pb).

1.2 - Dissertation Objectives

This dissertation aims to discuss the impact of industrial problems in CIGS thin-film solar cells performance.

Although the PV market is dominated by Si technology, CIGS thin-film cells have several advantages when compared to the former. The energy payback is much more advantageous and the versatility in the application of CIGS cells, due to the possibility of manufacturing flexible cells or on-demand geometry, are competitive advantages that this technology can bring to the market. Therefore, the identification of problems that may arise in the manufacturing process of CIGS thin films and the effects that they may have on their performance is of critical importance in the implementation of improvements both in the process and in the final product.

In the proposed project a plan for advanced characterization of the optoelectronic properties of CIGS cells will be implemented and executed. This analysis will be based on measurements of the electrical, current density vs voltage, temperature dependent current density vs voltage, light intensity dependent current density vs voltage, impedance spectroscopy and external quantum efficiency characteristics of a set of solar cells that will simulate possible fabrication problems. These cells will identify problems of (1) oxidation, i.e., O_2 contamination, a common problem in the handling/storage of the devices during fabrication, and (2) poor Na doping, which occur by application on low quality substrates or poor Na supply in the fabrication line. These results will be compared with a set of cells that do not exhibit the mentioned problems for benchmarking.

1.3 - Dissertation Structure

The present work is composed of five chapters, introduction, bibliographic review, processes and methodology, results and discussion and finally conclusion and future work.

The Introduction chapter aims to present the relevance of PV energy sources in today's world, followed by a brief description of how this type of technology works and how it has been developed.

In the second chapter, bibliographic review, the focus is placed on CIGS, presenting all the layers that constitute the cell, from its purpose to the electrical characteristics it must have.

The processes and methodologies explain the methods used to study the three devices presented in this chapter, and why some of these methods were chosen. All sections of the chapter provide a brief presentation of some experimental results and a general evaluation of the device in order to find defective cells and thus discard them from future studies.

The results obtained will then be meticulously analyzed, in Chapter 4, and discussed in order to understand the correlations between each of the electrical characteristics studied, associating them with each other in order to understand the consequences of each of them on the devices under study.

Finally, the conclusion contains what is considered the final comparison between each of the devices, pointing out the problems and advantages of each of them, and mentioning some methods that could be performed in the future in order to achieve a more complete evaluation of the devices.

CHAPTER 2

2 - Bibliographic Review

2.1 - CIGS Framework

CIGS is one of the absorber materials used within the second generation PV. The name CIGS come from the composition of its absorber layer, where four chemical elements are present, copper (Cu), indium (In), gallium (Ga) and selenium (Se), presenting a structure like that shown in Figure 4. The continued study of CIGS devices has led to a progressive improvement in efficiency over the years, with the 2017 record of 22.9% efficiency being surpassed in 2019 by the still current record of 23.35% (Nakamura et al., 2019). However, there is still a big difference between the values obtained in the laboratory and those possible for large-scale production, 19,2% (Photovoltaics report, 2022).

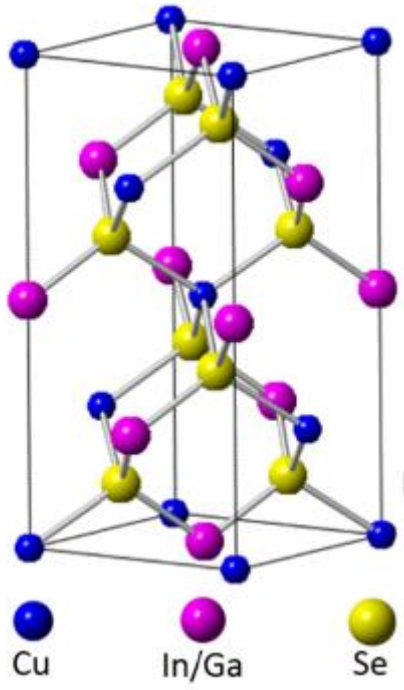

Figure 4 - $Cu(In,Ga)Se_2$ crystal structure, extracted from (Durgalakshmi et al., 2020)

CIGS solar cells have substrate based architecture that comprises 5 main layers, from top to bottom: window layer, buffer layer, absorber layer, back contact, and substrate (Giannazzo et al., 2022) organized according to the Figure 5.

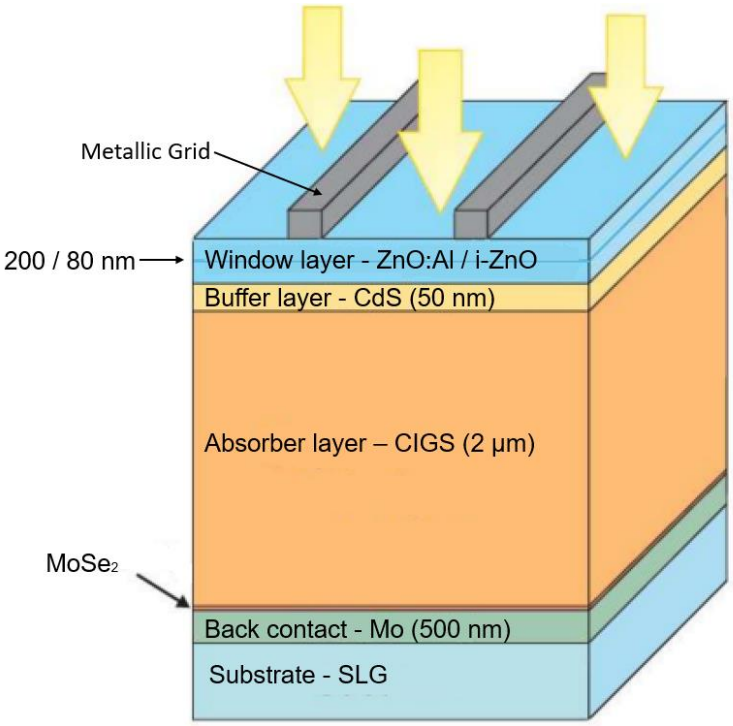

Figure 5 - Layer arrangement of a CIGS solar cell, adapted from (Salhi, 2022)

2.1.1 - Layers

1. Window layer: ZnO:Al and i-ZnO

The window layer is the first layer that makes up a solar cell, being deposited on top of the buffer layer, and its purpose is to collect the carriers and limit electronic losses.

It must then:

i) be conductive and, at the same time, prevent shunt paths;

ii) be optically transparent to reduce parasitic absorption;

iii) have a favorable band alignment with the buffer layer together with low recombination losses at the window/buffer interface

The most common system is a bilayer of aluminum-doped zinc oxide (ZnO:Al) and intrinsic zinc oxide (i-ZnO), the first layer being used because of its high conductive capacity and the latter used for the purpose of preventing shunts.

2. Buffer layer: CdS

The buffer layer is responsible for the formation of a p-n junction in a way that makes it possible to separate the electrical charges and generate power. It is also a protection against oxidation of the absorber layer.

To get the most out of a buffer layer, the ideal characteristics for the formation of this layer were described (Naghavi et al., 2010):

i. a wide bandgap (>3 eV);

ii. a suitable conduction band line-up to the absorber and to the window;

iii. a complete coverage of the surface, using a layer thinner than the current thickness of 70 nm of the CdS layer to further increase transparency;

iv. a deposition method that causes no surface damage to the absorber layer;

v. a good lattice match with the CIGS;

For CIGS based solar cells, the most adopted buffer layer is the CdS, by chemical bath deposition (CBD). The major advantages of this method are the ease of integration on a laboratory scale, and the ability to reconstruct the CIGS surface by removing oxides or fluorides present at the front surface. CdS follows the majority of the criteria above, except in point i), (bandgap of CdS is 2.4-2.5 eV) (Doiia & Herrero, 1997). Two other disadvantages are that CBD interrupts the vacuum process cycle and that CdS itself does not comply with the environmental standards present in certain markets, such as the European Union and Japan, since cadmium is considered to be toxic. For this reason, compounds such as ZnS, In_2S_3, Zn_xTi_yO, $Zn_{1-x}Sn_xO_y$, $Zn_{1-x}Mg_xO$, $In_x(OOH,S)$ and $Zn(O,S,OH)_x/Zn_{0.8}Mg_{0.2}O$ were evaluated, however these cannot be considered direct substitutes since they could not always overcome the efficiency levels provided by CdS (Nakamura et al., 2019).

In line with these ideas, the record of 23.35% efficiency was achieved in 2019, without the use of CdS, by replacing the conventional layer with the $Zn(O,S,OH)_x/Zn_{0.8}Mg_{0.2}O$ (Zn-based) double buffer layer. This exchange allowed the bandgap to reach 3.37eV, which respects the point i), leading to an increase in the external quantum efficiency (EQE) response, in comparison with CdS, which have a parasitic absorption in the 400 - 500nm range (Nakamura et al., 2019).

Although the purpose of this layer is to protect the absorber layer from oxidation, this doesn't always happen and oxidation is a recurrent phenomenon.

The impact of oxidation is still under debate, meaning that it is not possible to confirm its benefits or harms without further studies of the device, since the oxidation influence depends on all the deposition processes.

Research into the incorporation of O_2 into CIGS is extensive, and this has been pointed out as one of the ways to obtain high-performance PV cells. Oxidation may help to passivate defects in the grain boundaries and on the surface of the cell exposed to light, and has been proved capable of removing interface defects when it occurs on the CIGS surface. In the buffer/absorber interface, the air exposure presents convergences: on one hand, it reduces the recombination rates (Shin et al., 2015), allowing for more efficient collection of the photogenerated carriers; on the other hand, it causes the positive charge at the interface to decrease, leading to an increase in the holes available for recombination (Rau et al., 1999).

3. CIGS absorber layer

CIGS is the most important layer since it is the absorber layer, where the light must be absorbed allowing for electron-hole pair. CIGS is a chalcogenide, being the chalcogenide quaternary crystalline structure (Lee et al., 2010), illustrated in *Figure 4*, and it be seen that two of the four bonds of the Se atom are filled with In or Ga atoms, while the rest are filled with Cu atoms.

CIGS devices belong to the second generation, thin films solar cells, since CIGS is a direct bandgap material. This, allows to create an absorber with much lower thickness, in counterpart with Si (150 µm vs 2 µm). This bandgap has a limit between 1.04 eV (CIS) and 1.68 eV (CGS),

(Poortmans & Arkhipov, 2006), and it is possible to vary between these two values, by changing the In and Ga concentration.

Contrary to Si based solar cells, the CIGS is a self-doped material. The p-type doping comes from vacancies of Cu (V_{Cu}), mostly driven by its Cu poor composition required for highly efficient cells. The most widely used method for the deposition of this layer is co-evaporation as it allows the simultaneous evaporation of several materials under controlled vacuum conditions (Niki et al., 2010), thus enabling a controlled and homogeneous deposition. The co-evaporation process can be performed in different ways, depending on the number of steps it is divided into. The most extreme of the three is the single-stage process, which evaporates Cu, In, Ga and Se into a single step through high temperatures and has been used in the laboratory. Unlike the first, both the bi-layer and the three-stage co-evaporation have a Cu-rich period, which improves grain growth (Huang et al., 2018). The bi-layer process, both of which are performed on a substrate at high temperatures, where the first step is for Cu-rich growth and a second step where the film is converted to Cu poor composition. The more extensive three-stage process goes in the following sequence: i) a layer composed of In, Ga and Se grows on the back contact after evaporation of these same elements, ii) Cu and Se are evaporated at a higher temperature than previously used, resulting in the formation of a CIGS film, and iii) the In, Ga and Se elements are evaporated in the CIGS layer, causing it to become Cu-poor (Jung et al., 2010). The differences between these co-evaporation processes are illustrated graphically in Figure 6.

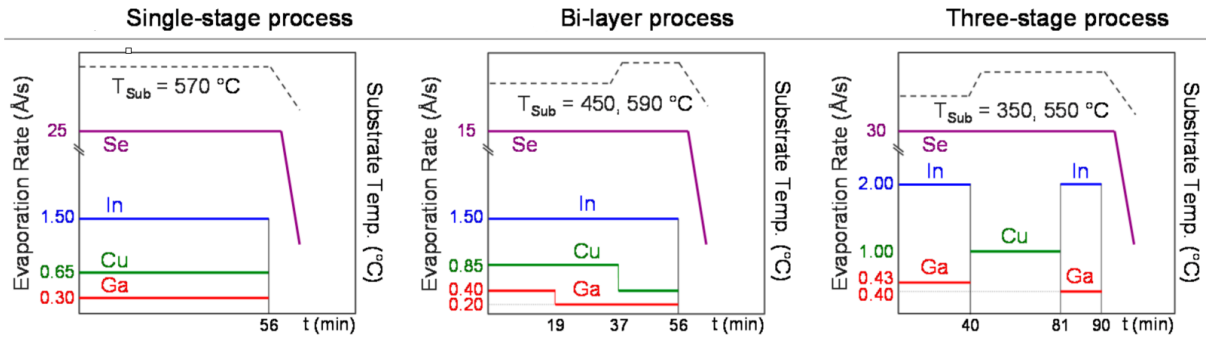

Figure 6 - Graphical comparison between the three co-evaporation processes, adapted from (Huang et al., 2018)

4. Back contact: Mo

Back contact layer is characterized by being a metallic layer on the back of the solar cell, and which is responsible for collecting the photo-generated holes into an external circuit. Two requirements must then be met, these being the provision of a low series resistance and an ohmic contact with the absorber layer. A quasi-ohmic with the conventional molybdenum (Mo) back contact only happens if it exists the formation of $MoSe_2$ (Wada et al., 2001) during CIGS growth deposition.

This type of contact can use many different materials depending on the type of PV technology it is embedded in, but in the case of CIGS cells the most common material is Mo, applied in a double layer configuration (Baek et al., 2023). This approach takes advantage of the characteristics of the metal, as its strong adhesion is useful for the deposition of the bottom layer and the high electrical conductivity fits perfectly with the need to have an ohmic low top layer. In addition, Mo is very resistant to both high temperatures and corrosion and is therefore very stable even when subjected to less favorable environments, such as the deposition conditions of the absorber layer, during which time it remains inert (Venkata Ratan, 2019). It also allows the diffusion of Na into the absorber layer without diffusing into it.

5. Substrate: SLG

The substrate is the layer represented lower down in the CIGS structure, shown in Figure 5, because its function is to provide structural and physical stability to the cell, as well as to ensure a smooth and flat surface for the subsequent deposition of the upper layers. Regarding the type of material that composes it, this can vary, and the most common is glass, since it has a very attractive low price, is available in large quantities, has a very stable behaviour over time, is considerably resistant and the fact that it is easy to handle, and mold allows it to be very adaptable since it can acquire a wide range of shapes and sizes.

Concluding then that glass is the right choice for non-flexible solar cells, one must take into consideration what type of glass should then be chosen to best fulfill the requirements. When analyzed the most used type of glass in CIGS is soda-lime glass (SLG) (Salomé et al., 2015). Although it is a common product, its cheap, high temperature resistance, electronic insulation, and the fact that it has a strain point of around 514°C, an annealing point of 550°C, a glass transition temperature of around 570°C, and a softening Littleton Point is at 720°C. This allows the SLG, when subjected to temperatures between 450-600ºC, the CIGS growth phase,

to pass through most of the aforementioned phases, thereby dramatically increasing ion mobility and allowing for diffusion of sodium (Na) ions into the absorber layer.

The benefits of Na doping are already well known, (Uppsala Universitet, 2011) have shown that small amounts of sodium significantly improve the efficiency of the devices, and even if there is an excess, these efficiencies will not decrease considerably, so this element is considered the most suitable for the development of CIGS (Contreras et al., 1997).

This efficiency improvement is primarily due to the fact that Na acts as an additional dopant in the p-type layer of the cell, causing both the open circuit voltage (V_{OC}) and the fill factor (FF) to increase (Yun et al., 2007). The diffusion of this element also makes it possible to increase the grain size and passivate the grain boundaries (Sozzi et al., 2021), as well as increasing the carrier density and the minority carrier lifetime (Salome et al., 2014), thus reducing recombination rates. If Na is lacking, there will be a decrease in the minority carrier lifetime, which in turn limits the V_{OC} and FF of the cell (Gunawan et al., 2010).

CHAPTER 3

3 - Processes and methodology

PV devices are fragile and can break or scratch quite easily, the results of the study depending on the condition of these devices, so precautions were taken when handling them.

All devices followed the same storage pattern, although CIGS solar cells are quite stable to long periods of light exposure, the existence of humidity can cause a significant degradation, like oxidation and interface deterioration, so they were stored in an exicator, closed environment, exposed to luminosity but which guarantees a low humidity level.

To avoid damaging or dirtying the devices, gloves and tweezers were always used when handling them, avoiding that either of these two utensils touched the surface of any of the cells.

Since CIGS has proven a beneficial reversible metastability under light soaking, all devices were subjected to 20 minutes of this process, before performing all the processes presented below, in order to obtain the most optimized electrical values possible, thus enabling a fairer comparison of results (Institute of Electrical and Electronics Engineers et al., 2011).

Below are presented each of the tests performed in their order of execution. Subsequently, the data generated by each test was analyzed promptly after its completion. This analysis process led to the gradual exclusion of cells from the study, since the aim is to identify a functional cell that is representative of the entire cell population in each device. This selection process was necessary due to the increasing complexity and time demands associated with the evolution of the tests.

3.1 - Devices characterization

The study focuses on understanding the electrical behaviour of three different devices: Reference device, oxygen (O_2) exposed device and Na free device. The set of devices is shown in Figure 7,with a total of 79 solar cells available for study, distributed among the devices as follows: 24 in the reference device, 24 in the device exposed to O_2 and 31 cells in the Na free device.

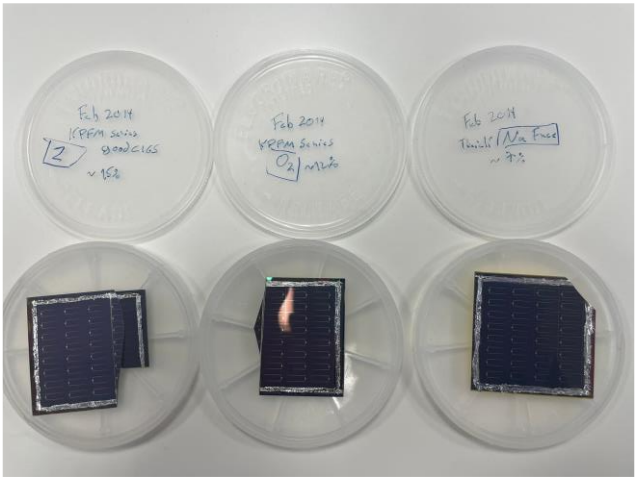

Figure 7 - The 3 devices and their cells, photo taken in the laboratory

In order to identify individual cells, an enumeration scheme applied which will be followed throughout the Thesis. The numbering starts in the top left corner of the device, increasing vertically downwards and developing towards the right side, with the cell in the bottom right corner having the highest number. The enumeration scheme is presented in Figure 8.

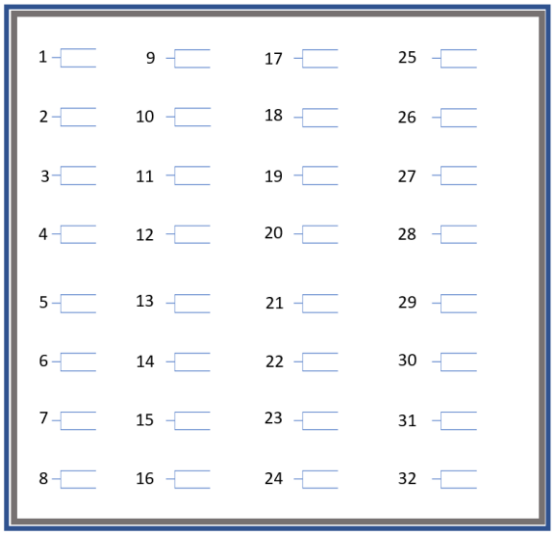

Figure 8 - Studied devices scheme with 32 individual solar cells enumerated

3.1.1 - Reference device

The reference device has a similar structure to the one shown in Figure 9, having already been described in detail in section 2.1.

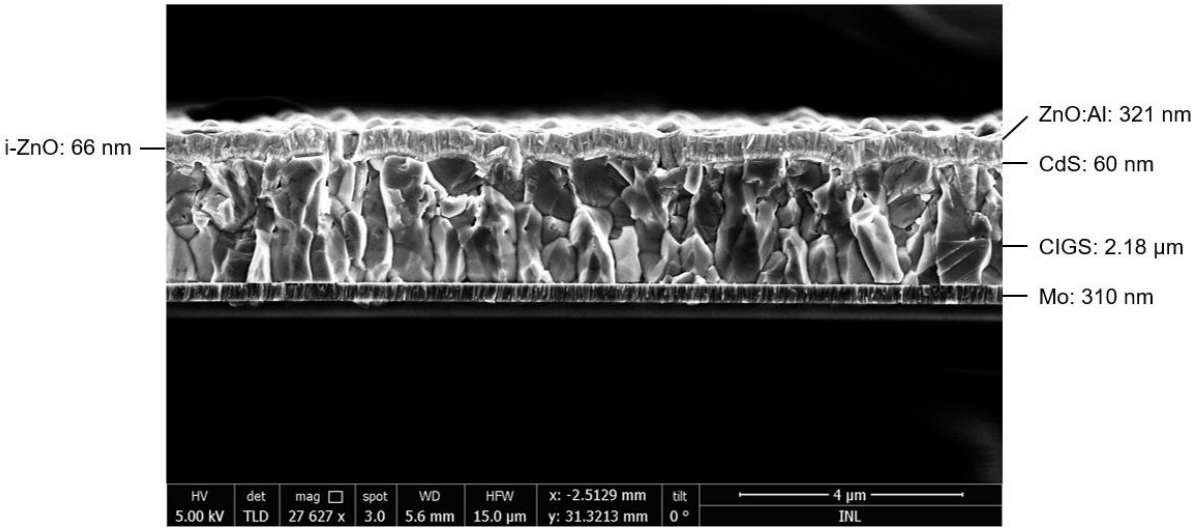

Figure 9 - SEM cross-sectional image of a representative solar cell from the Reference device

3.1.2 - O_2 device

The O_2 exposed solar cells follow the same architecture of the one from the reference ones , differing only in the fact that the CIGS layer was exposed to air for days and there was no immediate deposition of CdS, unlike the other two devices where the process took place in an inert gas atmosphere, which led to oxidation of the bulk.

3.1.3 - Sodium free device

The sodium free device differs from the reference device is the absence of sodium, and to completely eliminate this element it is necessary to change the SLG substrate, as this material is a source of Na (Sakurai et al., 2003), so the material used in the substrate of this device is sintered allumina. This device will then be compared with the reference one in order to study the impact of Na in a CIGS-type photovoltaic device.

3.2 - Current density vs voltage

The current density-voltage curve, represented in Figure 10, describes the dependence of the voltage on the current of solar cell. By studying this curve, it is possible to obtain important electrical

characteristics of the cell, such as open circuit voltage (V_{OC}), short circuit current density (J_{SC}), fill factor (FF) and from those parameters it is possible to determine the most standard figures of merit, the efficiency (ɳ), thus allowing discuss the performance of the solar cell. It is furthermore possible to indicate values such as maximum power point (M_P), current at maximum power point (J_{MP}) and voltage at maximum power point (V_{MP}).

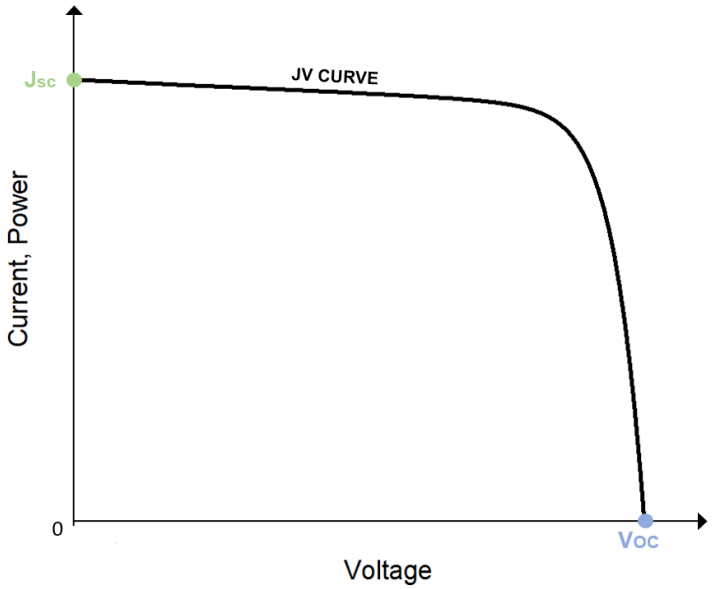

Figure 10 - Characteristic JV curve of a solar cell

It is even possible to detect problems in the cell taking into consideration the slopes present in the JV curve, since these same slopes represent the values of parallel resistance (R_P) and series resistance (R_S), Figure 11.

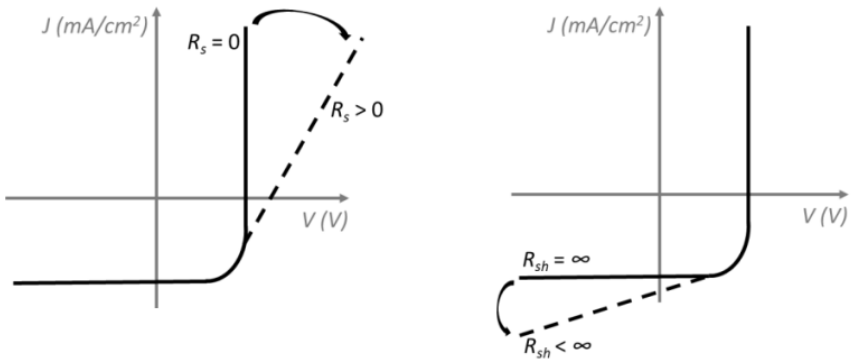

Figure 11 - Schematic illustrating the relationship between the JV curve and the parallel resistance (R_{sh}) and series resistance (R_s)

The aforementioned variables can be described as:

i. V_{OC}: Represents the difference in electrical potential generated between the terminals of the cell due to the absorption of light, under conditions of absence of current from an external circuit. Its value determines the maximum potential voltage that the cell can provide under ideal conditions, but it can vary with the variation in light intensity and temperature. The V_{OC} can be obtained as

$$Voc = \left(\frac{A*K*T}{q}\right) \ln \left(\frac{J_l}{J_o}\right) + 1 \quad (1)$$

where A, K, T, q, J_l and J_0 are ideality factor, Boltzmann constant, temperature, electron charge, photocurrent and dark saturation current respectively

ii. J_{SC}: It is one of the most important variables for classifying a solar cell . Its value shows the maximum amount of current that a cell is capable of supplying when the voltage between the terminals is equal to zero, i.e. when the cell is short-circuited and there is no resistance to the flow of current, which can be represented by

$$J(V = 0) = J_I = J_{SC} \quad (2)$$

iii. R_P: It is related to leakage currents at the edges of the cell, with a high R_P acting as a barrier against such leakage, so it should be as high as possible.

iv. RS: This consists of the sum of all the resistances in the system, from the semiconductor material to the electrical contacts. A solar cell should have the lowest possible resistance in series in order to avoid energy losses, thus increasing the efficiency of the device.

v. FF: Calculated using the equation 3,

$$FF = \frac{V_{mp} * J_{mp}}{V_{OC} * J_{SC}} \quad (3)$$

its value varies between 0 and 1, and it is common to convert it into a percentage. Describes the capacity of a photovoltaic cell to maintain an ideal ratio between its voltage and current.

vi. ɳ (efficiency): The most used variable to define the quality of a photovoltaic system, it expresses the percentage of useful electrical energy that can be produced from the total incident energy,

$$\eta = \frac{V_{mp} * J_{mp}}{P_{in}} = \frac{V_{OC} * J_{SC} * FF}{P_{in}} \quad (4)$$

P_{in} is the total energy reaching the cell, i.e. the intensity of the solar simulator/radiation

JV curve, Figure 10, will be obtained by exposing a solar cell to light conditions of 100 mW/cm2 according to the AM1.5G spectrum, JV light, and under dark, JV dark (S. S. Hegedus & Shafarman, 2004a).

The experimental work was done in a closed environment, with no light entering, the cells being exposed only to the Oriel LSH-7320 ABA LED Solar Simulator, which was calibrated before starting any measurement, by using a Si reference cell, ensuring the luminosity conditions mentioned above.

In order to carry out the JV light measurements in the most methodical way possible, a height adjustment of the solar simulator was made so that the light focus is always aligned with each of the cells to be studied, exposing the cell to 100 mW/cm^2 of irradiance, and obtaining more accurate results.

The next step is to place the probes tips on each of the contacts (+/-), two probe tips on each of the contacts, Figure 12, after this process a contact test is then run in order to check the good contact between the surfaces and so quality measures.

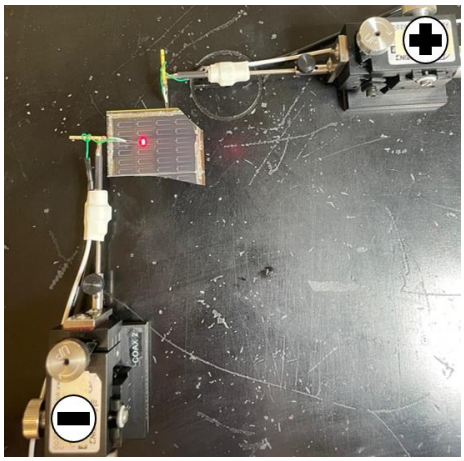

Figure 12 - JV setup and positioning of positive and negative contacts in the cell, photo taken in the laboratory

The IV_Measure.exe software was used to control and obtain data, using the variables shown in Figure 13.

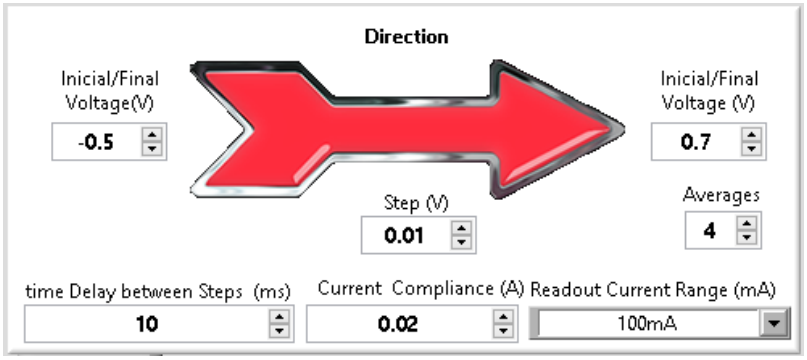

Figure 13 - Configuration of the IV_Measure.exe software and presentation of the variables used to perform the JV measurements

3.2.1 - Experimental data

Initially, an evaluation of the results was made using the values of JV behaviour, R_P and R_S of the cell as the main filters, whereby cells with abnormal JV curves (damaged cells), low R_P values and high R_S were removed from the study and not subjected to further tests.

These parameters were chosen since:

i. Damaged cells: Cells with JV behaviour different from the curve presented above have many defects associated with them, so they do not represent the functional set of devices in which they are inserted.

ii. Low R_P: If this value is too low, there tends to be a deviation of the current to the resistance in parallel, reducing the efficiency of the cell. It should also be noted that a low R_S can cause a difference between the current and the voltage of the circuit, causing the energy production to settle at a level below the maximum potential. Low values are generallY due to manufacturing problems.

iii. High R_S: In contrast to the R_P, R_S should be as low as possible in order to facilitate the current path through the cell. High R_S have a significantly negative effect on the FF and, in extreme cases, can affect the V_{OC}.

1. Reference device

From the obtained JV curves and considering the aforementioned constraints a total of 11 solar cells were discarded from the initial set of 24 from the reference device. Thus, the initial study will be focused on the 13 solar cells schematically presented in Figure 14.

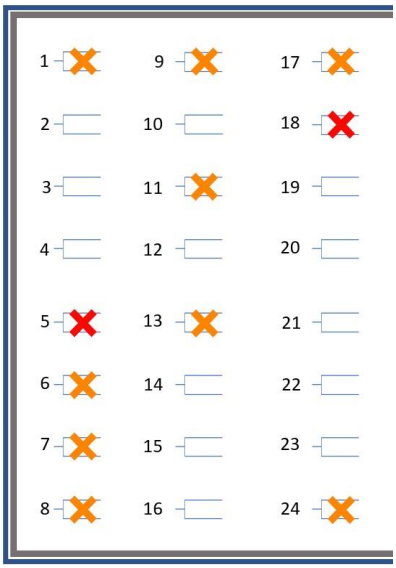

Figure 14 - Characterization of the problems and behaviours of the reference device **X**- cell with high R_S and/or low R_P **X**- cell with no photovoltaic behaviour (damaged)

All the remaining 13 cells present a common JV curve.

In Figure 15, is shown light and dark representative JV curves, where the light and dark curves are parallel to each other and show the desired exponentiality, without any visible shunt behaviour or any other kind of relevant deviations.

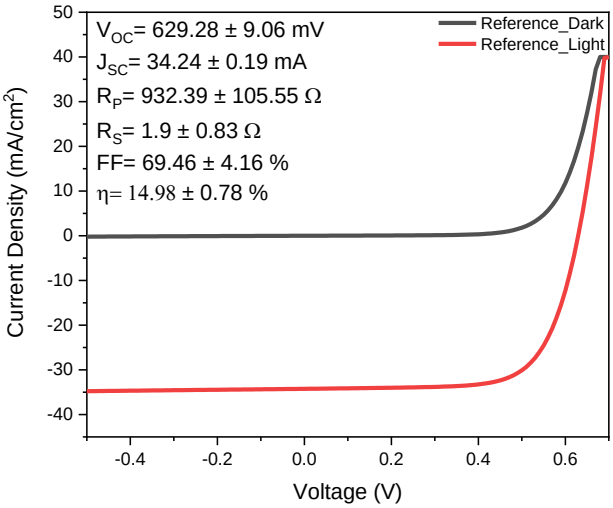

Figure 15 - Representative JV curve and electrical values of the reference device

2. O_2 device

Within the set of 24 cells present in the device exposed to O_2, 17 did not present significant problems so continued to be studied, while 7 were excluded, Figure 16.

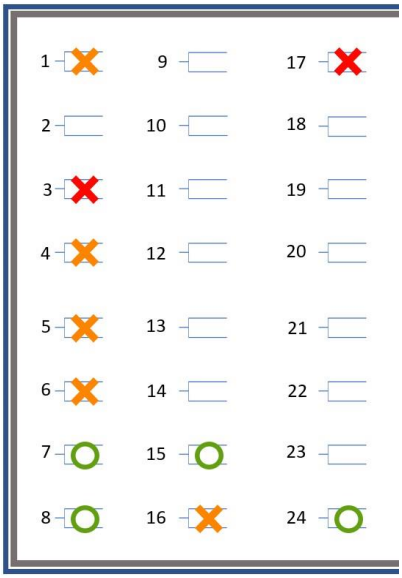

Figure 16 - Characterization of the problems and behaviours of the O_2 device **X**- cell with high R_S and/or low R_P **X**- cell with no photovoltaic behaviour (damaged) **O**- cell characterized by cross-over behaviour

The studied solar cells for O_2 device once it is possible to insert them in two distinct groups. Of these, 13 have a JV curve similar to those presented by the reference cells, while the other 4 present a cross-over, an interception between the JV light and JV dark curves, Figure 17.

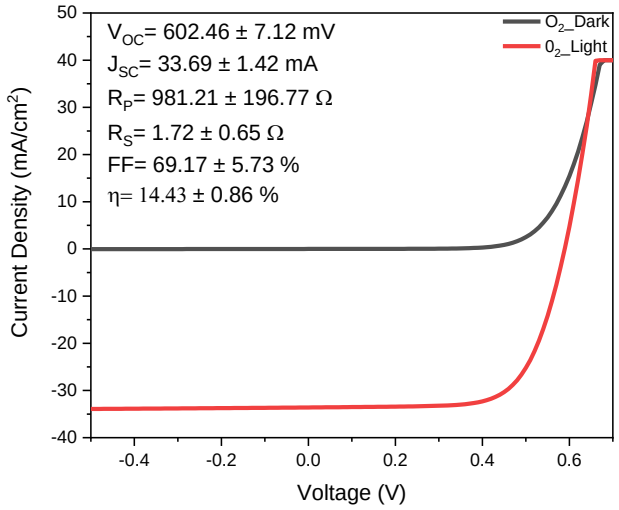

Figure 17 - Representative illuminate and dark JV curves and electrical values for a O_2 solar cell

Thin film cells often have cross-over points, at which point the dark and light voltage and current density are equal (Burgelman et al., 2000).

This is caused by the voltage dependent photocurrent, which can be due to an excessive carrier traps and recombination of carriers, thus forming electron barriers (Moore et al., 2014a). In addition to these factors, there is also the possibility that the cross-over is associated with low V_{OC} or FF values (S. Hegedus et al., 2007), which in the case of O_2 device can be ruled out since the values shown in Figure 17 differ only slightly from those of the reference device, Figure 15, where no cross-over occurs.

3. Na free device

The last device had a total of 31 cells, being the one with more cells eliminated due to the damaged state of the cells, 16 of which were removed, thus leaving 15 units to be studied in the Na free device, Figure 18.

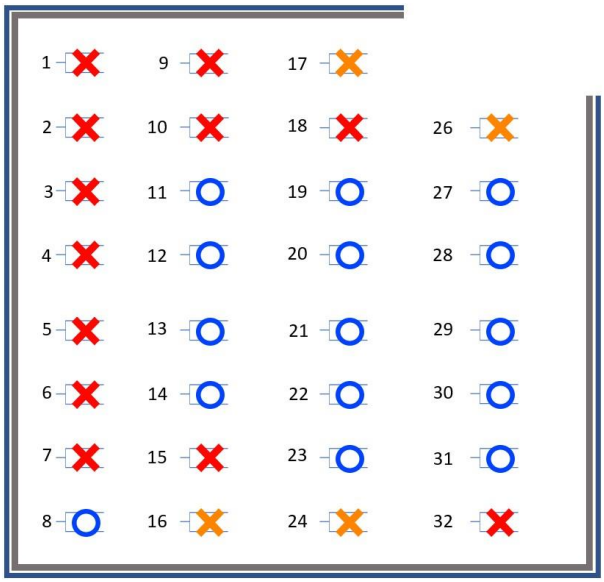

Figure 18 - Characterization of the problems and behaviours of the Na free device **X**-cell with high R_S and/or low R_P **X**- cell with no photovoltaic behaviour (damaged) **O**-cell characterized by cross-over and roll-over behaviour at the same time

Contrary to the reference and O_2 devices, none of the cells shows a characteristic JV curve as the one presented in Figure 10. All the curves obtained show both cross-over and roll-over effects, at the same time, Figure 19, common in cells with a lack of Na (Institute of Electrical and Electronics Engineers et al., 2011), so a low value is visible on the current density axis from the value 0.

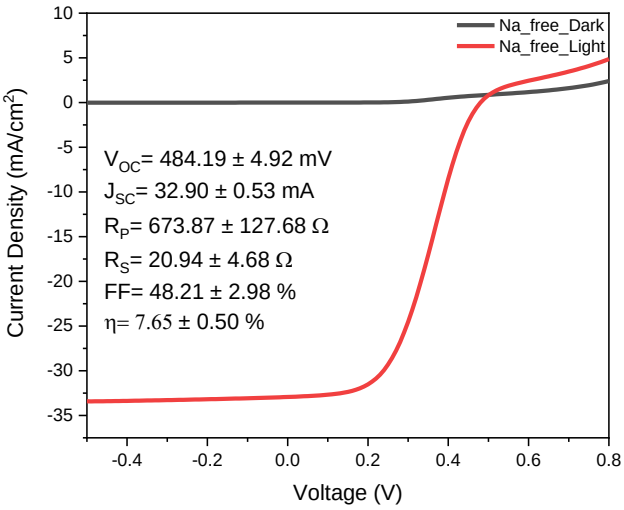

Figure 19 - Representative electrical values and JV curve of the Na free device showing simultaneous cross-over and roll-over behaviour

The roll-over behaviour is characterised by an abrupt decrease in energy conversion efficiency when the current density increases, commonly with the decrease in the slope of the JV light curve occurring in the area close to the V_{OC}.

Such behaviour is normally related to a barrier at the back contact of the cell, however, (Kephart et al., 2016) observed that it could also be caused by a large positive offset of the conduction band at the window/absorber layer interface. For a Na-free device, the cross-over would be more related to a barrier at the back contact.

The values obtained from the JV curve for each of the cells of each device are shown in Figure A1.

3.3 - Ideality factor

The ideality factor (A) quantifies how close the electrical behaviour of the cell is to the ideal behaviour defined by the diode equation:

$$J = J_l - J_0 \left[\exp\left(\frac{q * V}{A * K * T} \right) - 1 \right] \quad (5)$$

The value of A ranges between 1 and 2, with 1 being the ideal behaviour of the diode. However, the value of A is only equal to 1 if all recombination processes occur via traps in the bulk of the absorber or via band to band. As this does not happen in reality, since recombination occur in other ways and in other regions, the values of the cells studied will be higher than 1. To obtain this variable, the current density and voltage values used in section 3.1 were used.

Initially, this data was going to be transformed into dJ/dV vs V graphs, using both light and dark measurements, however, due to parasitic effects that affect the cells when they are under light, like voltage dependent current collection, which would cause the values obtained to be over-estimated (S. S. Hegedus & Shafarman, 2004), it was decided to only use the dark values, obtaining the value of the shunt conductance, G, at the point where V=0.

The shunt conductance represents the electric current that tends to deviate from the desired path in the electric circuit, thus becoming prejudicial to the cell reducing its efficiency since this current is not being used by the cell.

3.3.1 - Experimental data

Looking at the graphs obtained, Figure 20 a) shows reference device G value very close to 0 up to voltage values close to 0.4V, where there is exponential growth, which is the usual behaviour of a solar cell (S. S. Hegedus & Shafarman, 2004). This behaviour is very similar to that shown in Figure 20 b), which represents the O_2 device, although it has lower G values and a higher standard deviation. Finally, Figure 20 c) shows a completely different behaviour to the previous ones, with exponential growth beginning at lower voltage conditions, 0.2V, and this increase being interrupted by the formation of a parabola.

Since the method applied makes use of derivatives, cells that present cross-over and/or roll-over effects on JV curves are causing erroneous results, so it is not possible to make a comparison between the 3 devices.

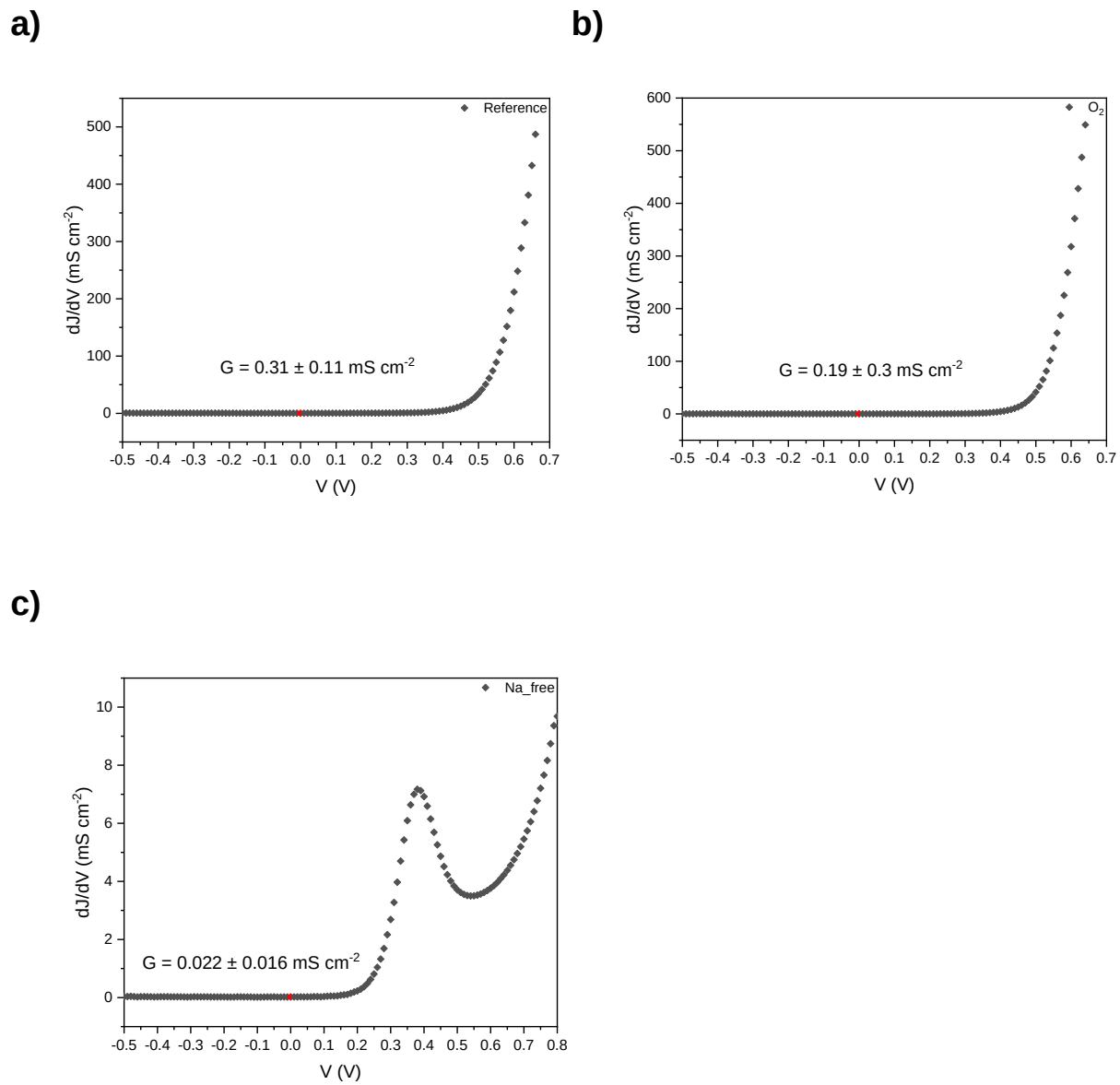

Figure 20 - dJ/dV vs V plot showing average values and standard deviations of the shunt conductance of each device a) reference device b) O_2 device c) Na free device

The obtained G then shows values that don't make sense in theory, previous graphs show that the devices with lower efficiencies have a much lower G than those with higher efficiencies, even though these are negatively affected by high shunt conductance.

These conclusions are further supported by the fact that both the O_2 and Na free devices showed very high % standard deviation, and that the cells belonging to the O_2 device that presented cross-over showed a very

high deviation of G when compared to the others, with these deviations being both above and below the average value, showing no consistency.

The method used to calculate the Ideality factor would be that demonstrated by (S. S. Hegedus & Shafarman, 2004b), after obtain the value of R_S, by plotting dV/dJ vs $(J+J_{SC})^{-1}$, with the second transformed into only J^{-1}, since under dark conditions $J_{SC}=0$.

The values of R_S and G would then be inserted into the equation:

$$J = J_0 * exp[(\frac{q}{A * K * T}) * (V - R_s * J)] + G_a * V - J_l \quad (6)$$

a comparative study between the devices will then be carried out and discussed later. Cells with higher A values that stood out negatively on the device should be discarded from future tests, but this was not possible as it was not possible to obtain realistic G values, which meant that correct A values could not be obtained.

The study of A will therefore be discarded from the results and discussion section since it is not possible to make a comparison between the three devices and the implication of their composition on the electrical behaviour of the solar cells.

3.4 - Quantum efficiency

The spectral response of a solar cell may be discussed through its quantum efficiency (QE). This parameter can be split in: internal quantum efficiency (IQE) and external quantum efficiency (EQE). IQE compares the collected charge carriers with the photons absorbed by the solar cell, i.e. the reflectance of the solar cell is not considered; while EQE compares the collected charge carriers with all the incident photons. Thus, EQE spectrum will provides an overall look to the optical losses. Moreover, from the EQE spectrum we may assess to other fundamental parameter: i) J_{SC} determined by integrating the EQE spectrum over the AM1.5 photon flux; and ii) the bandgap energies of the different layers in the solar cell.

An in-house built system, was used for the EQE measurements in the studies presented in this thesis. EQE was determined under ambient light, using chopped monochromatic light that was scanned through a wavelength range of 300-1100 nm with 5 nm steps.

Once all the adjustments have been made, the equipment is closed, so the only light in the space will be the beam emitted by the equipment itself.

3.4.1 - Experimental data

The graphs obtained through EQE measurements, Figure 21, show strong similarities between them, and the fact that due to equipment limitations it is not possible to extract the EQE for wavelengths longer than 1100 means that there are limitations in the analysis. It can be seen in Figure 21 that in the absorption zone between 400 and 500 nm there is a difference in behaviour between the 3 devices, indicating a possible difference in the thickness of the layer made up of CdS. It is also visible that the device that behaves a slightly differently from the others is the O_2 device, however all the devices show a higher EQE at values around 700 and 800 nm, i.e. in the red/infrared region.

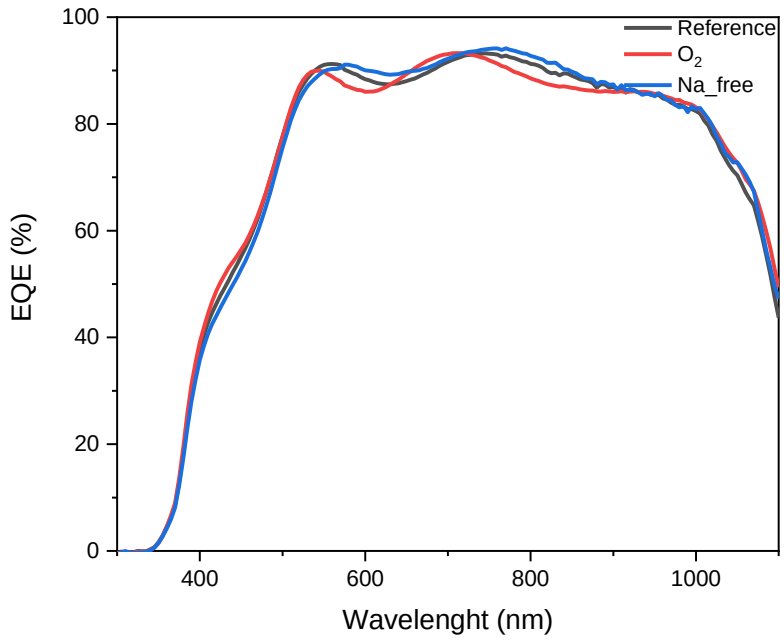

Figure 21 - Representative EQE spectrum for each studied device

The only cells that deviated from this standard were cell #4 of the reference device, showing a very low %EQE, despite a J_{SC} similar to the other cells, and cell #12 of the O_2 device as it failed to achieve stability in the EQE value meaning that no results could be obtained. For these reasons they were then discarded in the following studies.

Although it is not possible to draw very detailed conclusions from each of the devices in Figure 21, it is possible to extract the absorber

bandgap values for each of the cells. According to (Carron et al., 2019) there are 5 methods that allow absorber bandgap values to be obtained from EQE graphs, but only two have been taken into consideration, as the rest involve the use of other parameters such as the IQE and underestimate the bandgap values. These methods are:

i. Extrapolation to 0: Consists in the use of the slope present in one of the sections of the graphs obtained, making a linear regression of the points present in that area and extrapolating these values up to %EQE=0. This is a method that depends on the user, which may lead to different bandgap values from user to user.

ii. Derivative/inflection point: Using the expression $\left(\frac{d}{dE}\right) EQE$, a curve is generated from which the energy corresponding to the inflection point is taken as the bandgap value. Unlike the previous method, this one is user-independent, providing more an accurate value, with an average deviation from absorber of 5meV.

It was then decided to use the (ii) method in order to obtain the bandgap energy from the studied absorbers. The representative derivative plot of the EQE curve for the reference device is presented in Figure 22.

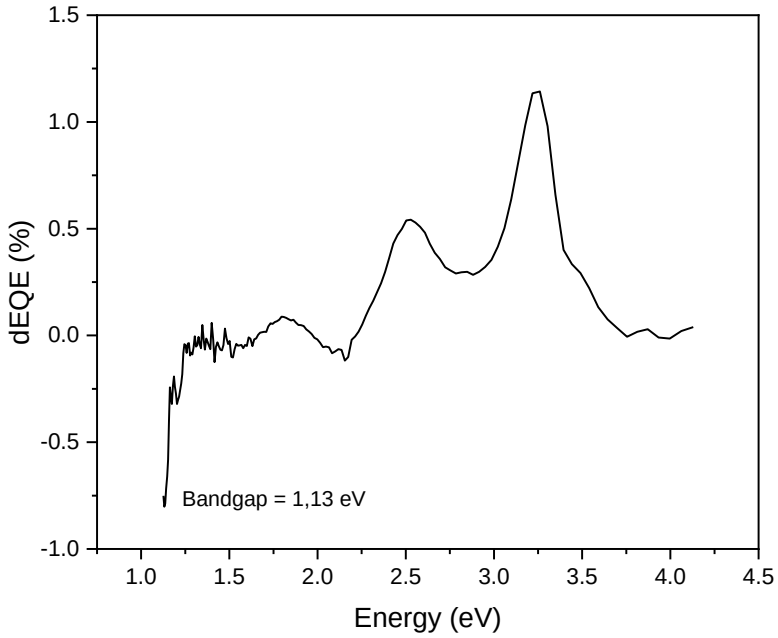

Figure 22 - Representative Derivative Graph of the EQE curve of a reference device
E (eV) = 1239.8 / λ (nm)

3.5 - Capacitance vs Voltage

From capacitance vs voltage (CV) measurements it is possible to obtain three fundamental characteristics of the PV device to be studied, built-in voltage (V_{bi}), net acceptor concentration (N_{CV}) and depletion region.

i. V_{bi}: It is the result of the voltage generated by the electric field in the depletion region, resulting from the potential difference between the p and n regions of the junction. Variable dependent on the concentrations of charge carriers present in both regions.

ii. N_{CV}: It represents the difference between the concentration of donors and acceptors, electrons and holes (Prokesch et al., 2002), with values as high as possible being desirable.

iii. Depletion region: A zone that surrounds the p-n junction and creates a barrier between the holes and the remaining electrons. Can be represented by a Kink in the energy band model, Figure 23.

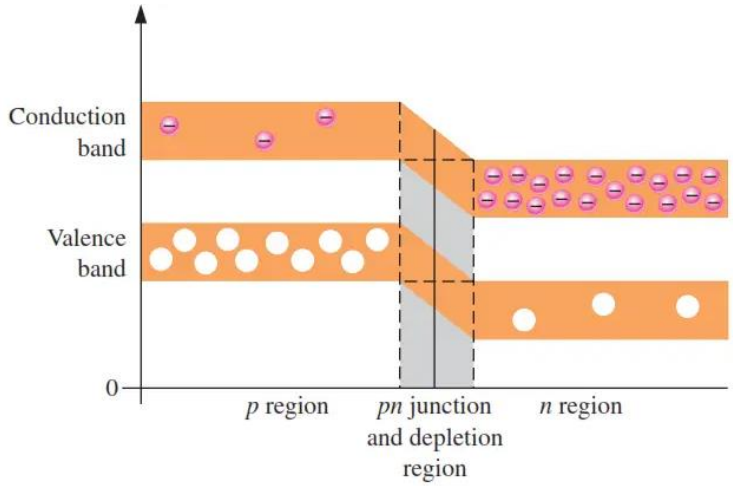

Figure 23 - Illustration of the depletion zone and its kink effect shown in an energy band diagram

The width of this region can be varied by applying voltage. If the junction is subjected to a positive voltage, the width of the depletion region will decrease, while the opposite will happen if the polarity becomes negative.

Capacitance values were obtained using devices such as LCR Meter and Source Meter, which in turn sent the data to the software "SpinMEMS_AC_Prober_v05".

Before any measurement, the LCR Meter was calibrated by open circuit measurements followed by short circuit measurements. All measurements were made in dark, under DC current, at a signal frequency = 10KHz and a signal level of 25 mV. A range was then defined between -0.8 and 0.7V, at which the LCR would measure capacitance.

3.5.1 - Mott-Schottky Plot

Mott-Schottky plot corresponds to a^2/C^2 VS voltage (S. S. Hegedus & Shafarman, 2004), and it is theoretically possible to obtain the net acceptor concentration using the slope value in the middle phase of the curve, as well as the V_{bi} using a linear regression in the last segment of the curve (Marlein & Burgelman, 2007), after a significant variation in slope, Figure 24.

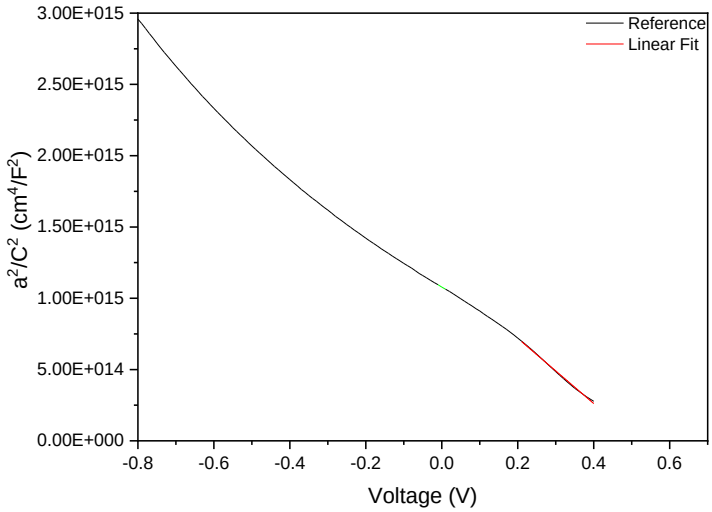

Figure 24 - Mott-Schottky Plot and obtention of V_{bi} through linear regression

At this stage, cell #20 of the reference cell was excluded from the study due to its behaviour, which differed from the others and was representative of electrical problems, presumably deterioration.

Even though it is theoretically possible to obtain the net carrier concentration from the graph in Figure 24, we opted to use the derivative method, as it is more accurate and allows us to analyse the graphical behaviour of each cell later.

3.5.2 - Derivative method

The derivative method is based on obtaining the N_{CV} values using the equations 7 and 8:

$$Ncv = \frac{2}{a^2 * q * \varepsilon} * \left(\frac{d * \left(\frac{1}{C^2}\right)}{dV} \right)^{-1} * 10^{-6} \text{ N/cm}^{-3} \quad (7)$$

Where a=0.00005 m^2, solar cell area, q=1.5E^{-19} C, electron charge, ε=1.2E^{-10}.

$$w = \left(\frac{A * \varepsilon}{C}\right) * 10^9 \text{ nm} \quad (8)$$

Even though all cells were subjected to a voltage range between -0.8 and 0.7V, only the region between -0.8 and 0.2V was used in the application of this method, since high positive voltages would excite the cell and erroneously affect the depletion region values. Higher positive voltage values should only be used in lower temperature cases, since only under these conditions do the results not depend on the voltage sweep (Ćwil et al., 2007).

1. Reference device

After the use of the derivative method, it was then possible to obtain the representative N_{cv} vs depletion region graphs of each cell. By comparing all the results, it was possible to classify the behaviour into two groups: Figure 25 a) initially shows a stable value, with an abrupt drop in the N_{CV} value when the distance to the interface exceeds 450 nm, while Figure 25 b) begins with a gradual increase in N_{CV} values all the way to 400 nm, where it reaches its peak, decreasing continuously from that point on, with a slope similar to the initial increase. The green dots represent the values of Voltage=0V. It can also be seen from Figure A2 that the cells exhibiting the behaviour shown in Figure 25 a) have higher Ncv values and lower depletion regions than the cells represented in Figure 25 b).

a) **b)**

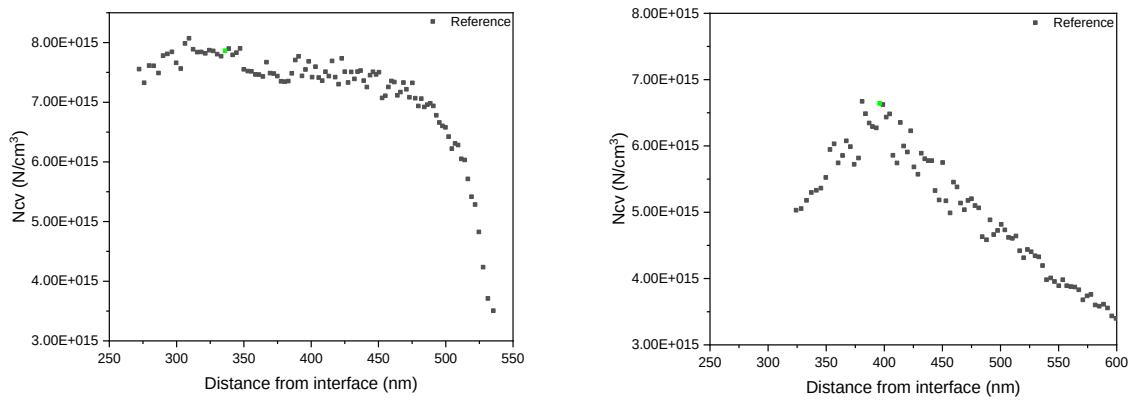

Figure 25 - Plot of the net concentration of acceptors vs. distance from the interface for the cells of the reference device a) cells: #2, #3, #10, #12 b) cells: #14, #15, #16, #19, #20, #21, #22, #23

2. O_2 device

As was done previously, the following Figure 26 a), b) and c) were chosen to represent the patterns shown by the device cells in a way that simplifies the interpretation of results. The only examples that do not follow these standards are cell #9 due to measurement problems, probably due to deterioration during its handling, and cell #2, represented in Figure 26 a), which because of its unique behaviour will be excluded from the study since it is no longer considered as a cell able to represent the device as a whole.

a) **b)**

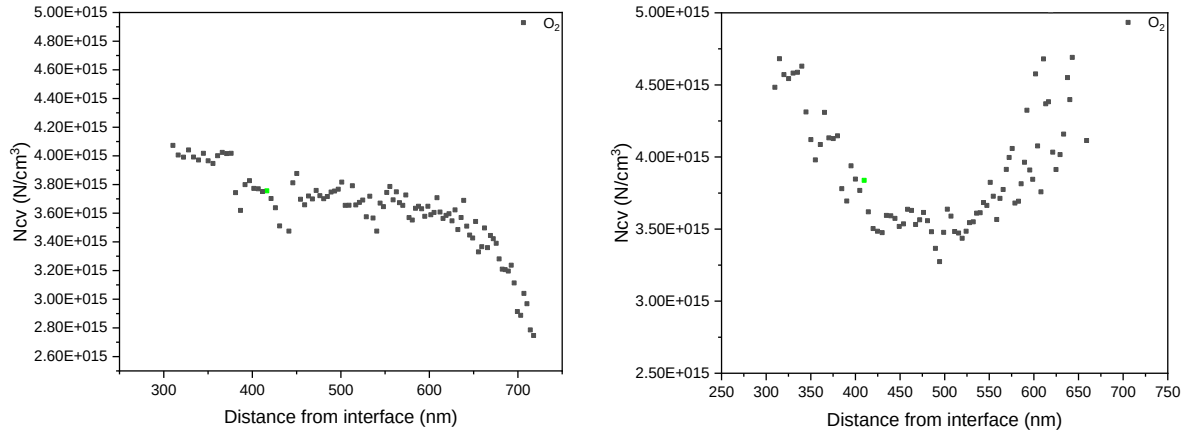

c)

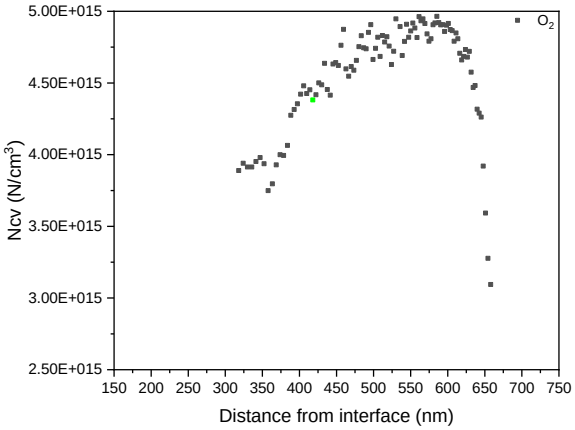

Figure 26 - Plot of the net concentration of acceptors vs. distance from the interface for the cells of the O_2 device a) cell #2 b) representative pattern of all cells that do not show cross-over, cells: #10, #11, #12, #13, #18, #19, #20, #21, #22, #23 c) cross-over cells pattern, cell: #7, #8, #15, #24

The main characteristic of Figure 26 b) is a curve with concavity facing upwards. The similarity to a parabola is, of all the behaviours observed above, the closest to the behaviours mentioned by several authors, such (Nardone et al., 2018), being visible in all the cells of the device that did not present cross-over.

In contrast, all 4 cells that had shown the cross-over effect, as shown in Figure 16, now exhibit in this test a behaviour opposite to the other cells, Figure 26 c), with the concavity in this case facing downwards.

3. Na free device

The device without sodium seems initially to have like the previous devices, two different characteristic patterns , Figure 27 a) and b), however it is possible to see that both graphs present certain similarities, such as:

i. They start with a similar decrease in N_{CV} values
ii. There is a slight increase near 0 V
iii. There is a start of increasing values near 2500 nm

For these reasons it will be considered that all cells follow this pattern, even though the curve presented in Figure 27 b) does not show as significant increase as the one present in Figure 27 a), it is considered that this does not happen due to the limitations on the distance from interface, being that it does not extend any further since it depends on the voltage values used in the tests.

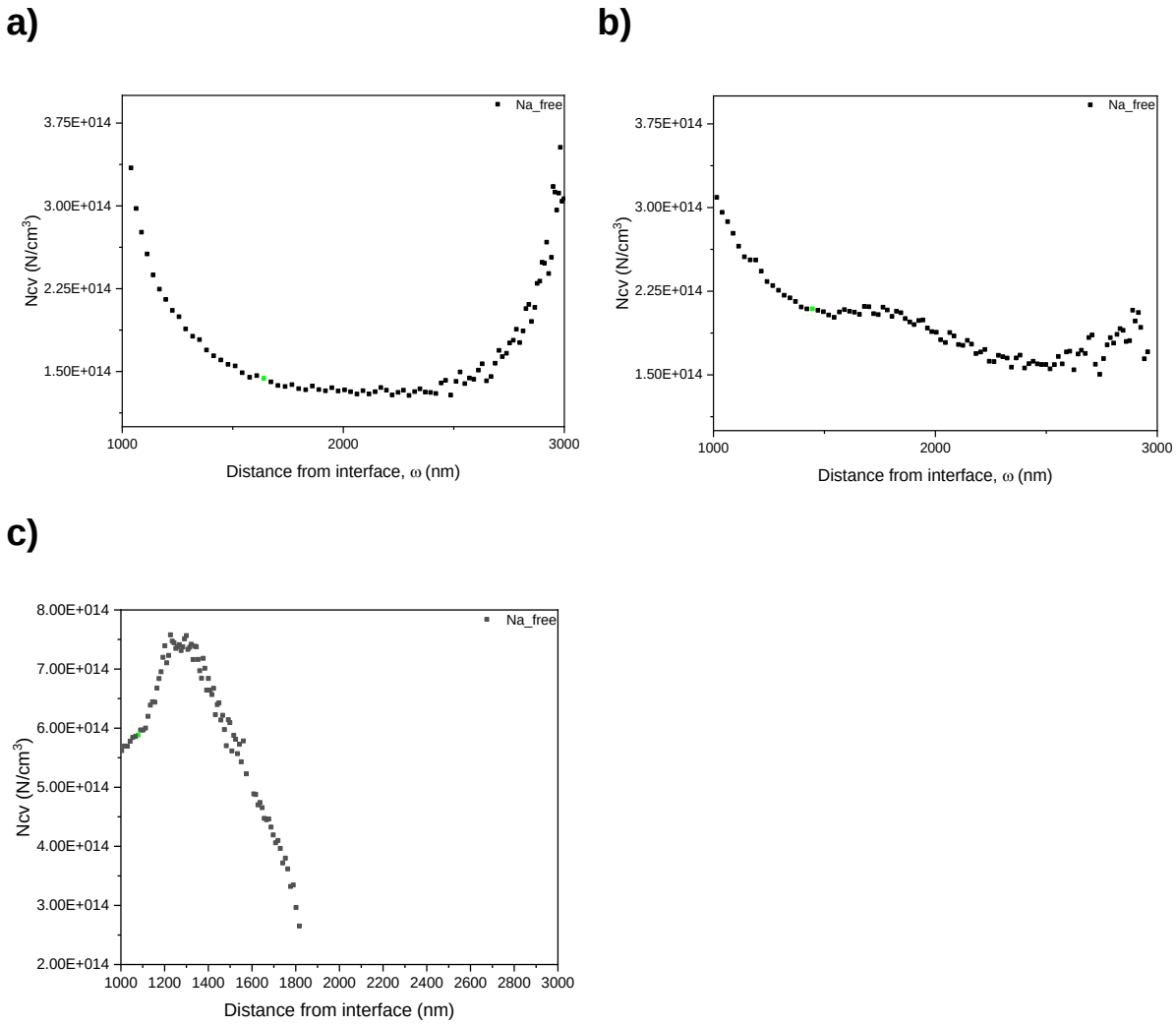

Figure 27 - Plot of the net concentration of acceptors vs. distance from the interface for the cells of the Na free device a) cells: #19, #20, #21, #27, #28, #29 b) cells: #11, #13, #14, #22, #23, #30, #31 c) cell #8

As with the other devices, cells will be discarded from the study. Cell 12 presented measurement problems and it was not feasible to obtain any kind of result, and cell #8 shows a unique behaviour, Figure 27 c), so it cannot be considered a representative cell of the device.

3.6 - Light intensity dependent current density vs voltage

The purpose of using light filters is to analyse the V_{OC} variation of the devices when they are exposed to different light intensities and wavelengths. This variation is subsequently used to understand and establish the values of the recombination coefficients in each regions of the cell (Abou-Ras et al., 2016), quasi-neutral region, R^b, depletion region,

R^d, and at the interface, R^i, which will be further divided into buffer/absorber interface, $R^{i,f}$, and absorber/back contact interface, $R^{i,b}$. Recombination process occurs when a hole and an electron combine, causing fewer free electrons to exist, thus decreasing the electric current generated by the cell.

For this study, neutral density filters were used as a way to vary the intensity of light incident on the cell, without changing the light spectrum. Since there were only five filters available, two adjustments were made in the solar simulator so that we could use these filters both at 100 mW/cm^2 and 50 mW/cm^2, thus making it possible to obtain more points in the graphs under study. The filters were placed one at a time above the solar cell with the help of a support, at a height of 3.5 cm with an inclination of 30º. In order to know the transmittance of each of the filters in this setup, a light intensity measurement was then made using the same silicon reference cell. These values are mentioned in Table 1.

Table 1 - Transmittance of light filters

Filter name	Transmittance
ND 1	81.43
ND 3	42.42
ND 5	33.13
ND 10	11.36
ND 20	1.05

To ensure that the device was only illuminated by light that passed through the filter, an opaque, thick, black cardboard structure was developed in the shape of a square pyramid, open at the base and cut in a region near the top, which was attached to the light source, Figure 28 a) and b) so that no light in the environment could reach the cell without passing through the filter.

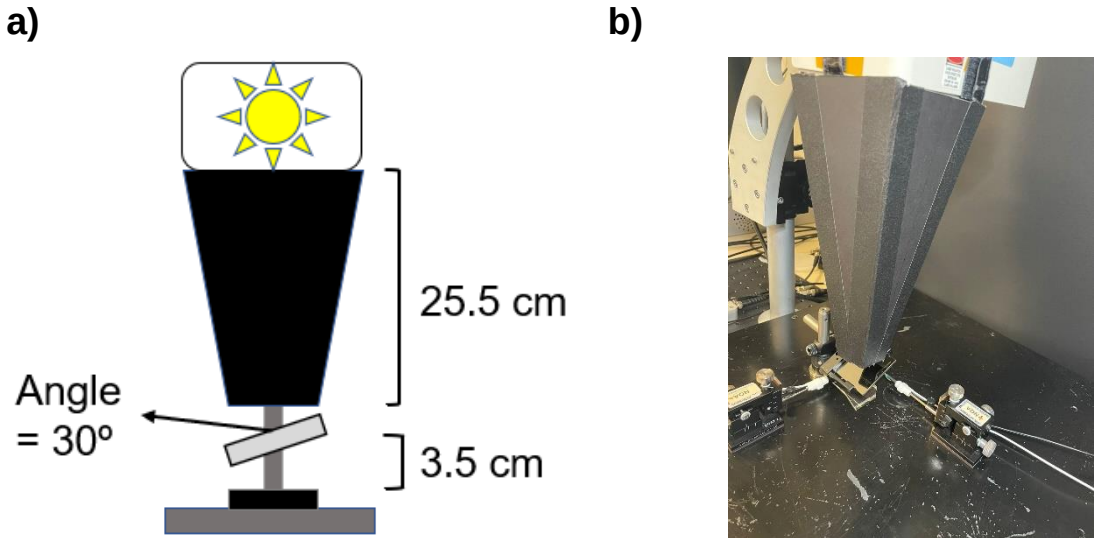

Figure 28 - Layout of the setup used for JV filter measurements a) vertical schematic of the setup showing measurements and angles used to assemble it b) picture of the setup

3.6.1 - Experimental data

The obtained data then needs to be transformed into V_{OC} vs light intensity, G_a, graphs, and a fit to the obtained curve with equation 9 was performed .

$$Voc = \left(\frac{2*K*T}{q}\right) \ln\left[K_1 * \left(\sqrt{(G_a * K_2 + 1)} - 1\right)\right] \quad (9)$$

From this adjustment is taken K_1, a dimensionless ratio that represents the impact of the recombination that occurs in the depletion region over the total of all the other recombination mechanisms that exist in the solar cell, can be defined by:

$$K_1 = \frac{1}{2} * \frac{R^d}{R^{i,f} + R^b + R^{i,b}} \quad (10)$$

and K_2, a dimensional ratio expressed in $Suns^{-1}$ that relates the recombination mechanisms to the thickness of the absorber layer (W) and can be defined by equation 11:

$$K_2 = \frac{4W * \left(R^{i,f} + R^b + R^{i,b}\right)}{(R^d)^2} \quad (11)$$

values that will be used for the calculation of the recombination coefficients mentioned above.

The Figure 29 a), b) and c), all present a behaviour in agreement with that predicted in (Paul et al., 2018) being possible the fit of the equation 9, however the cell #18 of the cell exposed to O_2, Figure 29 d),previously considered as one of the representative cells of the device did not fit this model.

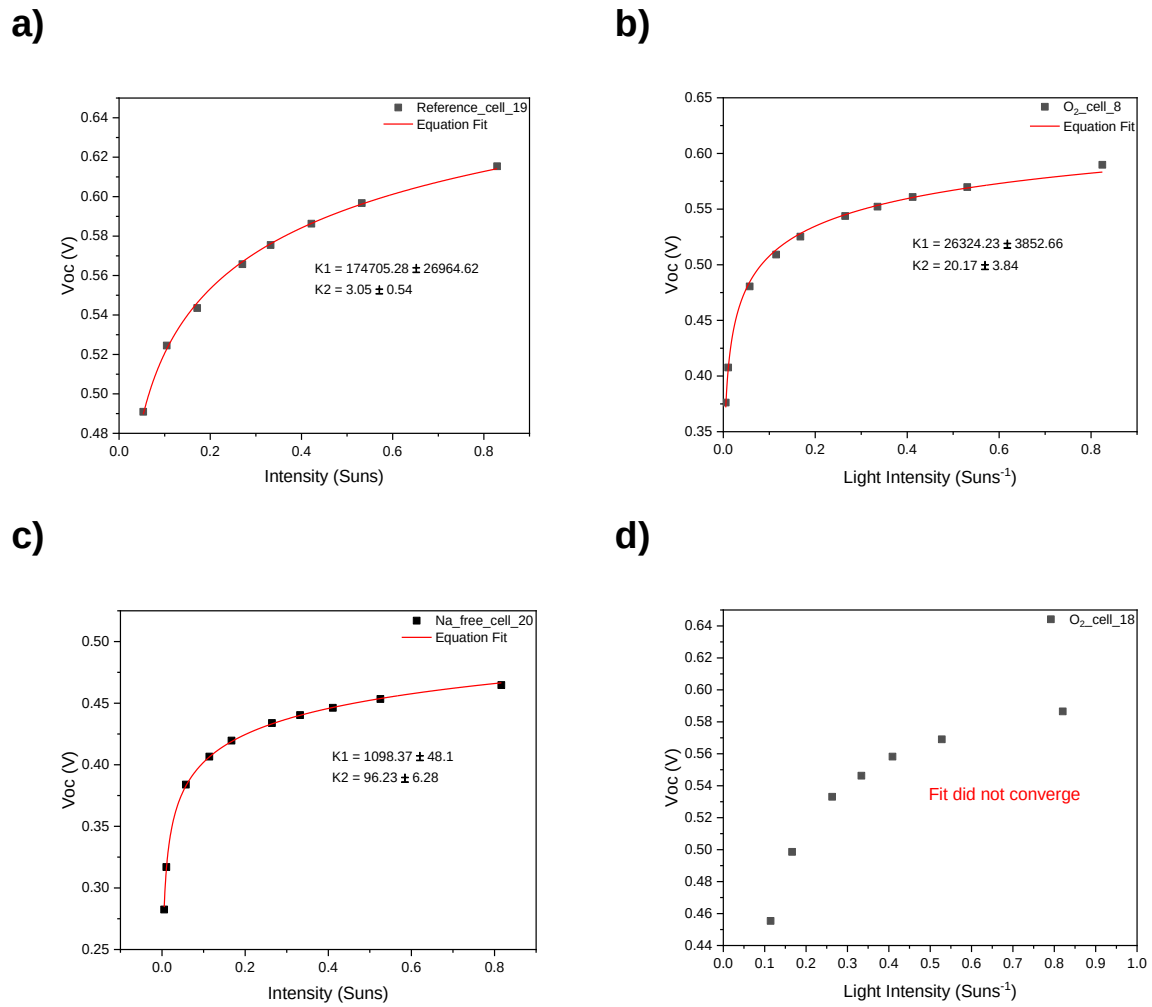

Figure 29 - Open circuit voltage vs light intensity plot a) reference cell #19 b) cell #8 exposed to O_2, shows cross-over c) Na free cell #20 d) cell #18 exposed to O_2, normal JV behaviour

In order to verify the results obtained, a J_{SC} vs G_a graph was then plotted, Figure 30 since the variation that these two variables show direct proportionality between them if there are no measurement errors (Hartnagel & Kirchartz, 2020).

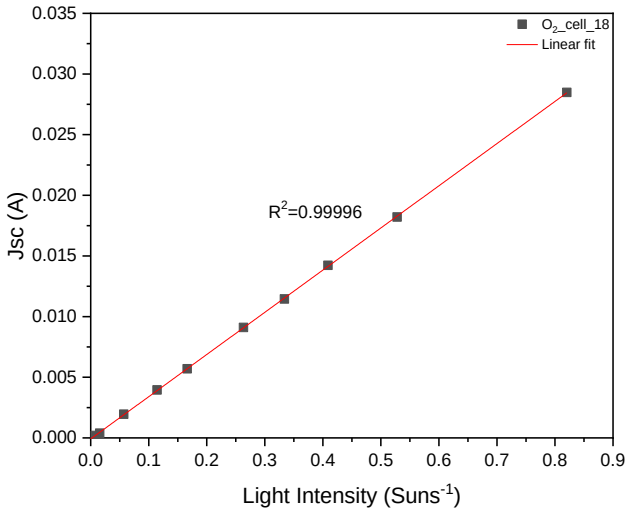

Figure 30 - Relation between short-circuit current and light intensity of cell #18 of the O_2 device based on linear regression

Thus, it is possible to observe through Figure 30 that there is a linear behaviour, which means that the adjustment problems observed earlier are due to problems with the cell and not problems during the measurements, making it impossible to continue studying the cell. The same study was then carried out on cell #19 of the O_2 device since it presented a representative behaviour, obtaining the same results as in the previous one. It was then considered that cells of the device exposed to O_2 that did not show the cross-over effect could not be studied using this approach since it is not possible to obtain the values of the K_1 and K_2.

In addition to the limitation presented above, there is another factor that will limit the study of recombination, since none of the three cells that presented fit, respect the $K_2*G_a>1$ law, which means that it will not be possible to study back contact, and so we decided not to perform complementary measurements with color filters, which would allow us to change the wavelength incident on the cell. Without this step it is no longer possible to deconvolute the recombination coefficient R^i into $R^{i,f}$ and $R^{i,b}$, so $R^i=R^{i,f}$ since white light fail to probe the recombination at absorber/back contact interface (Paul et al., 2018).

3.7 - Temperature dependent current density vs voltage

Since solar cells are sensitive to temperature, with variations in temperature resulting in a change in most of the parameters of the

semiconductor material, it is then used, as a complement to the study of the JV curve previously performed, the study of the temperature-dependent current-voltage curve (JVT). This is used to understand the recombination activation energy (Ea) of J_0 (Pettersson et al., 2009). This approach allows for a better understanding of de device's interfaces, and overall recombination mechanism which are limiting the solar cell performance.

In this study, the temperature variation was set between 293 and 143ºK, with JV measurements being taken every 10ºK.

Since this type of measurement is performed in a small environment, it is no longer possible to use the entire set of cells present in the devices, making it necessary to individualize them. This individualization is done by making a cut using a diamond-tipped pen, in order to create a cleavage line, then forcing the cell in that area to allow the cleanest possible break without compromising the condition of the cells that are intended to be studied.

The first step was to clean the silver block, used as device holder as well as heating block, using a soft cloth soaked in IPA (iso-propyl alcohol). Special attention was given to this step, since any kind of dirt could mean an air gap between the heating block and the device, resulting in temperature errors.

Finally, the device is placed on the heating block, connecting the probes to the respective contacts (+/-) Figure 31 a), followed by a purge in order to remove all water vapor from inside the equipment Figure 31 b), avoiding the danger of precipitation inside the chamber and thus deterioration of the cell.

a) **b)**

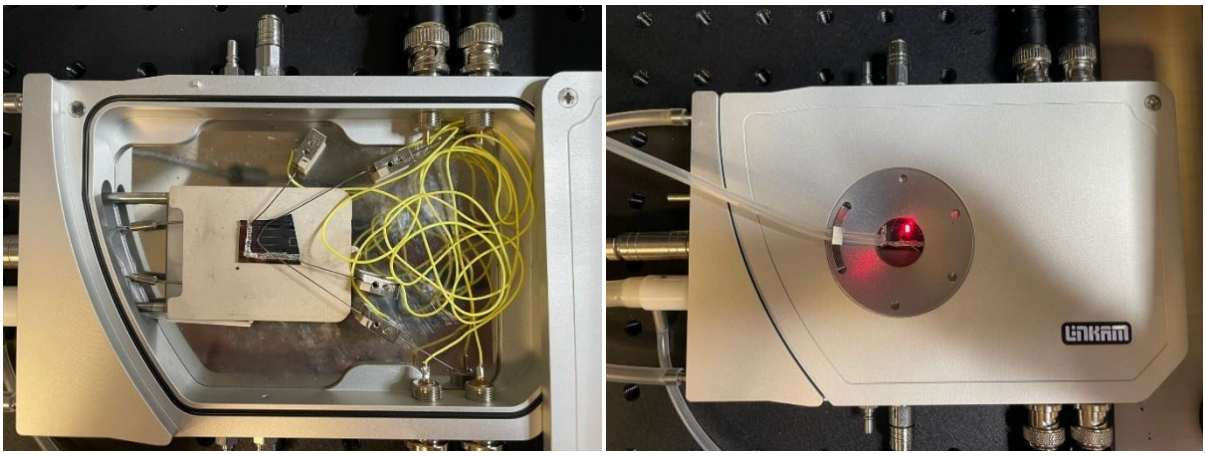

Figure 31 - Procedure for placing the cell in the cooling equipment to carry out JVT measurements a) open chamber, placing the cell and connecting the electrical contacts b) closed chamber, necessary condition to start the purging process

The temperature variation of the system is done through a liquid nitrogen cooling pump system, as N_2 allows temperatures as low as 143K to be reached. The temperature variation will occur uniformly at the rate of -5K/min, as a higher rate could lead to degradation of the cell.

After the temperature reaches the stipulated limit of 143K , it is run at that temperature for a period of 5 minutes to ensure that the entire cell area is at the same temperature. Thereafter, the temperature of the heating block is progressively increased, fixing the temperature at each point where a JV measurement is to be performed.

To verify the accuracy of the measurements and the existence or not of degradation of the cell during the process, the V_{OC} value at 293K is taken at first, before cooling it, being this procedure repeated, again at 20K, after the cell has been subjected to temperature variation. The existence of cell degradation is then rejected if the two values are similar or very close.

3.7.1 - Experimental data

The data analysis process is based on a V_{OC} (V) vs Temperature (K) plot, whereupon a linear regression is performed in order to obtain the energy value at T=0K.

It is necessary, however, to evaluate the values obtained in the JVT measurements, since in the first phase of the temperature decrease, the V_{OC} obtained tends to increase significantly, but the closer the

temperature gets to zero, the smaller the difference between the V_{OC} values obtained. Understanding this behaviour is important as the linear regression must be performed in the temperature range where the variation in open circuit voltage is highest. These range restrictions were only necessary for the cases in Figure 32 a) and b),

a)

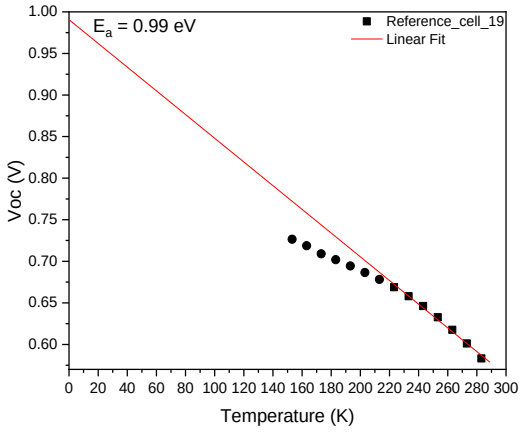

b)

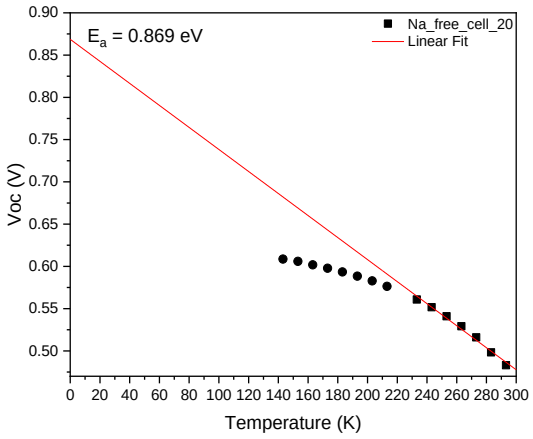

c)

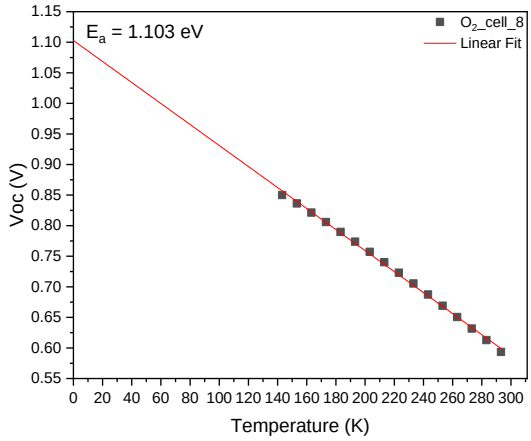

Figure 32 - Open circuit voltage vs temperature plot a) reference cell #19 b) Na free cell #20 c) cell #8 exposed to O_2

Because in the case of the cell exposed to O_2, Figure 32 c), the V_{OC} slop is nearly identical over the entire process, this is also the case in which the activation energy is the highest among the 3 devices.

CHAPTER 4

4 - Results and discussion

The obtained figures of merit from JV curves, Table 2, reveal the highest efficiency value for the reference device. Nevertheless, the efficiency value of the O_2 device is very close to the one obtained for the reference, being even within its standard deviation. On the other hand, a significant loss in the V_{OC} and FF values for Na free device led to a drop of close to 50 % in its efficiency value

One of the main characteristics of the cells exposed to O_2 when compared to the reference device is that all their parameters are lower, making the device less efficient, showing that air exposure of the CIGS layer has a harmful impact in the devices, despite the fact that presents a higher R_P and lower R_S. Another important piece of information is that the J_{SC} value is lower than that of the reference device, which is in line with (Shin et al., 2015) that predicts this effect on the solar cell after exposure to air.

As mentioned in section 2.1.1, the lack of Na was reflected in the lowest V_{OC} and FF values among all the devices, although these are not the only problems. The existence of roll-over, meaning the presence of barriers on back contact junction, in all the cells resulted in the device having the worst values in all the electrical parameters analysed so far. In order to address this significant loss on the V_{OC} value the bandgap energy needs to be addressed.

Table 2 - Results obtained through JV measurements, averages and standard deviations

Device	V_{OC} (mV)	J_{SC} (mA)	R_P (Ω)	R_S (Ω)	FF (%)	Ef (%)
Reference	629.28 ± 9.06	34.24 ± 0.19	932.39 ± 105.55	1.90 ± 0.83	69.46 ± 4.16	14.98 ± 0.78
O_2	602.46 ± 7.12	33.69 ± 1.42	981.21 ± 196.77	1.72 ± 0.65	69.17 ± 5.73	14.43 ± 0.86
Na free	484.19 ± 4.92	32.90 ± 0.53	673.87 ± 127.68	20.94 ± 4.68	48.21 ± 2.98	7.65 ± 0.50

The derivative method applied to the values obtained through the EQE spectrum shows equal bandgap values between the reference and O_2 devices, Table 3, and a slightly higher value for the sodium-free device. The fact that it was obtained a higher bandgap value for the Na free solar cells regarding the reference and O_2 ones, highlights even more the V_{OC} losses, suggesting that Na doping has a significant impact in passivation of recombination mechanisms

It should be noted that the values shown in Table 3 are within the range defined in chapter 2.1.1 for CIGS devices, 1.04 eV (CIS) and 1.68 eV (CGS). The values obtained indicate that the cells studied have an absorber constitution closer to CIS, with a low concentration of Ga.

Table 3 - Average and standard deviation of the absorber layer bandgap energy values of the different solar cells

	Reference device	**O_2 device**	**Na free device**
Bandgap (eV)	1.13 ± 1.8E-2	1.13 ± 3.2E-3	1.153 ± 1.7E-2

The previous difference in V_{OC} results can now be compared with V_{bi} results obtained from the Mott-Schottky plot, Table 4. This table shows agreement with (Manda et al., 2018), since V_{OC} and V_{bi} are related, we can consider the V_{bi} values adjusted to the study cases, since as happened with the V_{OC}, the reference device has the highest V_{bi} value and the Na free device has the worst result among all the devices. However, there is a big difference between the V_{bi} values of the O_2 device and the reference device, something that didn't happen with the V_{OC}.

According to (Moore et al., 2014), cross-overs can be caused by low V_{bi}, but when looking at the data, the four cells in the device exposed to O_2 show values that are even higher than the device average, with an average V_{bi} of 0.47V. On the other hand, the device without Na, which has the lowest V_{bi} values of all, is characterized by roll-over and cross-over behaviour in all the cells that compose it. Although these behaviours are not directly linked to low built-in voltage values, the V_{bi} difference of more than 200 mV between the reference device and the one without Na is specifically due to the lack of this element, since this factor decreases the carrier density, causing a lack of doping which in turn will affect the V_{bi} values (Salome et al., 2014).

Table 4 - Average and standard deviation of the built-in voltage of different devices

	Reference device	**O_2 device**	**Na free device**
V_{bi} (mV)	536.83 ± 38.75	421.26 ± 47.68	325.84 ± 79.81

Table 5 shows a relationship between the values of net acceptor concentration and the width of the depletion region, so that when the first decreases the second increases.

Table 5 - Net acceptor concentration and depletion region width values, obtained through C-V tests, when V=0

	Reference device	**O_2 device**	**Na free device**
Average Ncv (0V)	6.64E15 ± 7.36E14	3.50E15 ± 6.57E14	2.09E14 ± 1.16E14
Average Depletion region (0V)	386 ± 33.29	416 ± 28.28	1.47E3 ± 1.97E2

The N_{CV} values of the reference device are close to those of the O_2 device, while the Na free device has much lower values. This sequence of values agrees with (Cunha et al., 2021), which states that N_{CV} values increase with Na concentration, so the difference in values between the Na free device and the others is justified.

On the other hand, wider depletion regions are typically associated with an easier charge carrier collection, since they would be closer to the electrical contacts, which would make the cell more efficient, which is not the case for the studied cells.

After defining the photovoltaic cells that will be used to be representative of each of the devices, the highest Ea of 1.103 eV was obtained in the cell #8 exposed to O_2, while the lowest is present in the cell #20 Na free with a value of 0.869 eV with the reference cell #19 having an activation energy of 0.990 Ev.

The O_2 cell #8 shows an Ea very close to Eg, an indication that the most dominant recombination pathway is in the bulk, causing the V_{OC} to be limited by recombination in this zone (Elanzeery et al., 2018).

The remaining devices have activation energies considerably lower than the absorber bandgap, suggesting that the recombination that take place in the cell occur predominantly in buffer/absorber interface (Larsson et al., 2017) (Gunawan et al., 2010).

Recombination coefficients were studied using the same three cells as in the JVT measurements. Initially, the hole potential barrier was extracted by:

$$q * \varphi_{bO} = q * V_{bi} + \xi b \tag{12}$$

where ξb is the bulk Fermi level above valance (J. V. Li et al., 2014), extracted from average SCAPS.

The photon flux, pf, used is determined by the bandgap energy of each of the cells (Paul et al., 2018) and is then used to obtain the recombination coefficient in the depletion zone, according to the expression:

$$R^{\mathrm{d}} = (\frac{2 * pf}{K^1 * K_2}) \tag{13}$$

this coefficient is sequentially applied to intermediate calculations, the total of the recombination coefficients at the buffer/absorber interface and the quasi neutral region:

$$R^i + R^b = \frac{R^d}{2 \times K_1} \tag{14}$$

below is the second intermediate formula, which allows the value of R^b to be obtained, based on previously calculated variables:

$$\frac{R^i}{R^b} = \frac{Ea - Eg}{\varphi b_0 - Ea} \tag{15}$$

with the aforementioned values, the recombination coefficient in the quasi neutral region is calculated, which will subsequently also be used to obtain R^i,

$$R^b = \frac{R^i + R^b}{1 + \left(\frac{R^i}{R^b}\right)} \tag{16}$$

finally, it is possible to obtain the recombination coefficient in the buffer/absorber interface using the equation:

$$R^i = \left(R^i + R^b\right) - R^b \quad (17)$$

The numerical results of all the calculations presented above are shown below in Table 6.

Table 6 - Summary of the results obtained during the study that were used to obtain the recombination coefficients

	Reference Cell #19	**O_2 Cell #8**	**Na free Cell #20**
K_1	1.74E5	2.63E4	1.1E3
K_2	3.05	20.2	96.23
Photon flux (photons*cm^{-2}*s^{-1})	2.71E+17	2.71E+17	2.65E+17
V_{bi} (V)	5.37E-1	5.0E-1	3.7E-1
φb_0 (eV)	6.87E-1	6.5E-1	5.2E-1
Eg (eV)	1.13	1.13	1.15
Ea (eV)	9.9E-1	1.1	8.69E-1
R^d (cm^{-2}*s^{-1})	1.02E12	1.02E12	5.02E12
R^b (cm^{-2}*s^{-1})	1.99E6	1.83E7	1.27E9
R^i (cm^{-2}*s^{-1})	9.18E5	1.09E6	1.02E9

The results show that the reference cell has the lowest recombination coefficient values in all the zones studied. The cell that has been exposed to air shows results very close to the previous one, and the depletion zone even has similar results, with the biggest difference being located in the quasi neutral region, which supports (Elanzeery et al., 2018), verifying a very intense recombination pathway in the bulk, which explains the difference in V_{OC} between the two devices.

In contrast to the reference cell, the one without Na shows the worst results in all regions, with much higher recombination coefficient values than the others. The fact that this cell has a higher recombination coefficient in the depletion region than the sum of all the coefficients of each of the others is probably the most important factor for its limitations in open-circuit voltage, since these coefficients are one of the biggest loss mechanisms in photovoltaic equipment (Gunawan et al., 2010).

CHAPTER 5

5 - Conclusions and future work

5.1 - Conclusions

The purpose of this thesis is to characterise and evaluate solar cells which, due to manufacturing processes, are subject to non-ideal conditions. The studied devices comprised reference cells, manufactured under ideal conditions, which were compared with cells that the absorber layer have been exposed by O_2 and cells that the absorber have a lack of Na doping.

The relevance of this study lies in the fact that it allows the identification of problems connected to each of the manufacturing issues, understanding how much and in what way each of the variables in this process affects the performance of the final solar cell.

It was concluded that both devices produced in conditions different from the reference or ideal ones show worse results than those obtained in these conditions. Devices that suffer O_2 contamination during their deposition process present the possibility of barriers forming at the absorber/buffer interface, which are visible through cross-over behaviour. These devices present a lower charge carrier concentration than the reference device, as well as a higher recombination coefficient in quasi-neutral region, the oxidised zone, resulting in this device presenting slightly lower efficiency values than the reference devices. As for the lack of Na, this is the biggest problem since the lack of this element will inhibit the passivation of grain defects, resulting in the formation of barriers at the absorber/buffer and back contact/absorber interfaces. The devices without Na have the worst electrical figures of merit in all the areas studied, low charge carrier concentration and NCV and much higher recombination coefficients than the other devices in all 3 regions of the solar cell studied, resulting in a final efficiency of only 50% of the efficiency of a reference device.

5.2 - Future work

Future research could include the use of SEM to obtain cross-sectional images of the three devices, facilitating an in-depth examination of the grain structures in each. In addition, an interesting avenue of research would involve carrying out CV measurements at varying frequencies, followed by circuit fitting. This approach would serve to overcome the limitations associated with recombination at the absorber/back contact interface, thus allowing a comparative analysis between the devices studied.

BIBLIOGRAPHICAL REFERENCES

Abou-Ras, D., Kirchartz, T., & Rau, U. (2016). *Advanced characterization techniques for thin film solar cells*.

Archer, M. D., & Green, M. A. (2014). *Clean Electricity from Photovoltaics*. *4*. https://doi.org/10.1142/P798

Baek, M. C., Jang, J. S., Suryawanshi, M. P., Karade, V. C., Kim, J., He, M., Park, S. W., Kim, J. H., & Shin, S. W. (2023). Rear interface engineering via a facile oxidation process of Mo back contact for highly efficient CZTSSe thin film solar cells. *Journal of Alloys and Compounds*, *935*. https://doi.org/10.1016/j.jallcom.2022.167993

Burgelman, M., Nollet, P., & Degrave, S. (n.d.). *Modelling polycrystalline semiconductor solar cells*. www.elsevier.com/locate/tsf

Carron, R., Andres, C., Avancini, E., Feurer, T., Nishiwaki, S., Pisoni, S., Fu, F., Lingg, M., Romanyuk, Y. E., Buecheler, S., & Tiwari, A. N. (2019). Bandgap of thin film solar cell absorbers: A comparison of various determination methods. *Thin Solid Films*, *669*, 482–486. https://doi.org/10.1016/j.tsf.2018.11.017

Chapin, D., & Fuller, C. (n.d.). *The Silicon Solar Cell Turns 50*.

Chen, H., Jeong, S. Y., Tian, J., Zhang, Y., Naphade, D. R., Alsufyani, M., Zhang, W., Griggs, S., Hu, H., Barlow, S., Woo, H. Y., Marder, S. R., Anthopoulos, T. D., McCulloch, I., & Lin, Y. (2023). A 19% efficient and stable organic photovoltaic device enabled by a guest nonfullerene acceptor with fibril-like morphology. *Energy & Environmental Science*. https://doi.org/10.1039/D2EE03483B

Contreras, M. A., Egaas, B., Dippo, P., Webb, J., Granata, J., Ramanathan, K., Asher, S., Swartzlander, A., Noufi, R., & Contreras, M. A. (1997). *On the Role of Na and Modifications to Cu(In,Ga)Se 2 Absorber Materials Using Thin-MF (M=Na, K, Cs) Precursor Layers*.

Cunha, J. M. V., Oliveira, K., Lontchi, J., Lopes, T. S., Curado, M. A., Barbosa, J. R. S., Vinhais, C., Chen, W. C., Borme, J., Fonseca, H., Gaspar, J., Flandre, D., Edoff, M., Silva, A. G., Teixeira, J. P., Fernandes, P. A., & Salomé, P. M. P. (2021). High-Performance and Industrially Viable Nanostructured SiOx Layers for Interface Passivation in Thin Film Solar Cells. *Solar RRL*, *5*(3). https://doi.org/10.1002/solr.202000534

Ćwil, M., Igalson, M., Zabierowski, P., Kaufmann, C. A., & Neisser, A. (2007). Capacitance profiling in the CIGS solar cells. *Thin Solid Films*, *515*(15 SPEC. ISS.), 6229–6232. https://doi.org/10.1016/j.tsf.2006.12.102

Doiia, J. M., & Herrero, J. (1997).); (b) E. Guti6rrez-Rios, Quimica Inorgdni-ca. In *The Electrochemical Soci-ety Proceedings Series* (Vol. 144, Issue 11). JCPDS International.

Durgalakshmi, D., Balakumar, S., Rajendran, S., & Naushad, M. (2020). Functional nanomaterial in energy and environmental science. *Nanomaterials for Sustainable Energy and Environmental Remediation*, 1–23. https://doi.org/10.1016/B978-0-12-819355-6.00001-7

Elanzeery, H., Babbe, F., Melchiorre, M., Werner, F., & Siebentritt, S. (2018). High-performance low bandgap thin film solar cells for tandem applications. *Progress in Photovoltaics: Research and Applications*, *26*(7), 437–442. https://doi.org/10.1002/pip.3026

Enkhardt, S. (2022, July 13). *Trina Solar achieves 24.5% efficiency for 210 mm p-type PERC solar cell – pv magazine International*. https://www.pv-magazine.com/2022/07/13/trina-solar-achieves-24-5-efficiency-for-210-mm-p-type-perc-solar-cell/

Giannazzo, F., Shtepliuk, I., Goubard, F., & Salhi, B. (2022). The Photovoltaic Cell Based on CIGS: Principles and Technologies. *Materials 2022, Vol. 15, Page 1908*, *15*(5), 1908. https://doi.org/10.3390/MA15051908

González-Eguino, M. (2015). Energy poverty: An overview. In *Renewable and Sustainable Energy Reviews* (Vol. 47, pp. 377–385). Elsevier Ltd. https://doi.org/10.1016/j.rser.2015.03.013

Green, M. A., Dunlop, E. D., Hohl-Ebinger, J., Yoshita, M., Kopidakis, N., Bothe, K., Hinken, D., Rauer, M., & Hao, X. (2022). Solar cell efficiency tables (Version 60). *Progress in Photovoltaics: Research and Applications*, *30*(7), 687–701. https://doi.org/10.1002/pip.3595

Gunawan, O., Todorov, T. K., & Mitzi, D. B. (2010). Loss mechanisms in hydrazine-processed Cu2 ZnSn (Se,S) 4 solar cells. *Applied Physics Letters*, *97*(23). https://doi.org/10.1063/1.3522884

Hartnagel, P., & Kirchartz, T. (2020). Understanding the Light-Intensity Dependence of the Short-Circuit Current of Organic Solar Cells. *Advanced Theory and Simulations*, *3*(10). https://doi.org/10.1002/adts.202000116

Hegedus, S., Desai, D., & Thompson, C. (2007). Voltage dependent photocurrent collection in CdTe/CdS solar cells. *Progress in Photovoltaics: Research and Applications*, *15*(7), 587–602. https://doi.org/10.1002/pip.767

Hegedus, S. S., & Shafarman, W. N. (2004a). Thin-film solar cells: Device measurements and analysis. *Progress in Photovoltaics: Research and Applications*, *12*(2–3), 155–176. https://doi.org/10.1002/pip.518

Hegedus, S. S., & Shafarman, W. N. (2004b). Thin-film solar cells: Device measurements and analysis. *Progress in Photovoltaics: Research and Applications*, *12*(2–3), 155–176. https://doi.org/10.1002/pip.518

Huang, C. H., Chuang, W. J., Lin, C. P., Jan, Y. L., & Shih, Y. C. (2018). Deposition technologies of high-efficiency cigs solar cells: Development of two-step and co-evaporation processes. *Crystals*, *8*(7). https://doi.org/10.3390/cryst8070296

Institute of Electrical and Electronics Engineers, IEEE Electron Devices Society, IEEE Photovoltaic Specialists Conference 37 2011.06.19-24 Seattle, Wash., & PVSC 37 2011.06.19-24 Seattle, Wash. (2011a). *37th IEEE Photovoltaic Specialists Conference (PVSC), 2011 19 - 24 June 2011, Seattle, Washington ; conference proceedings*. IEEE.

Institute of Electrical and Electronics Engineers, IEEE Electron Devices Society, IEEE Photovoltaic Specialists Conference 37 2011.06.19-24 Seattle, Wash., & PVSC 37 2011.06.19-24 Seattle, Wash. (2011b). *37th IEEE Photovoltaic Specialists Conference (PVSC), 2011 19 - 24 June 2011, Seattle, Washington ; conference proceedings*. IEEE.

Jacobo, J. (2022, November 21). *LONGi sets 26.81% efficiency record for heterojunction solar cells - PV Tech*. https://www.pv-tech.org/longi-sets-26-81-efficiency-record-for-heterojunction-solar-cells/

Jung, S., Ahn, S. J., Yun, J. H., Gwak, J., Kim, D., & Yoon, K. (2010). Effects of Ga contents on properties of CIGS thin films and solar cells fabricated by co-evaporation technique. *Current Applied Physics*, *10*(4), 990–996. https://doi.org/10.1016/j.cap.2009.11.082

Kephart, J. M., McCamy, J. W., Ma, Z., Ganjoo, A., Alamgir, F. M., & Sampath, W. S. (2016). Band alignment of front contact layers for high-efficiency CdTe solar cells. *Solar Energy Materials and Solar Cells*, *157*, 266–275. https://doi.org/10.1016/j.solmat.2016.05.050

Khan, Z., Elahi, A., Bukhari, D. A., & Rehman, A. (2022). Cadmium sources, toxicity, resistance and removal by microorganisms-A potential strategy for cadmium eradication. In *Journal of Saudi Chemical Society* (Vol. 26, Issue 6). Elsevier B.V. https://doi.org/10.1016/j.jscs.2022.101569

Kumari, N., Kumar Singh, S., & Kumar, S. (2022). A comparative study of different materials used for solar photovoltaics technology. *Materials Today: Proceedings*, *66*, 3522–3528. https://doi.org/10.1016/j.matpr.2022.06.403

Larsson, F., Nilsson, N. S., Keller, J., Frisk, C., Kosyak, V., Edoff, M., & Törndahl, T. (2017). Record 1.0 V open-circuit voltage in wide band gap chalcopyrite solar cells. *Progress in Photovoltaics: Research and Applications*, *25*(9), 755–763. https://doi.org/10.1002/pip.2914

Lee, E., Cho, J. W., Kim, J., Yun, J., Kim, J. H., & Min, B. K. (2010). Synthesis of CIGS powders: Transition from binary to quaternary

crystalline structure. *Journal of Alloys and Compounds*, *506*(2), 969–972. https://doi.org/10.1016/j.jallcom.2010.07.131

Lin, L., & Ravindra, N. M. (2020). CIGS and perovskite solar cells-an overview. *Emerging Materials Research*, *9*(3), 812–824. https://doi.org/10.1680/jemmr.20.00124

Li, J. V., Grover, S., Contreras, M. A., Ramanathan, K., Kuciauskas, D., & Noufi, R. (2014). A recombination analysis of Cu(In,Ga)Se2 solar cells with low and high Ga compositions. *Solar Energy Materials and Solar Cells*, *124*, 143–149. https://doi.org/10.1016/j.solmat.2014.01.047

Li, Z., Qiu, F., Tian, Q., Yue, X., & Zhang, T. (2022). Production and recovery of tellurium from metallurgical intermediates and electronic waste-A comprehensive review. In *Journal of Cleaner Production* (Vol. 366). Elsevier Ltd. https://doi.org/10.1016/j.jclepro.2022.132796

Manda, P. K., Ramaswamy, S., & Dutta, S. (2018). Extraction of the built-in potential for organic solar cells from current-voltage characteristics. *IEEE Transactions on Electron Devices*, *65*(1), 184–190. https://doi.org/10.1109/TED.2017.2773708

Marlein, J., & Burgelman, M. (2007). *ELECTRICAL PROPERTIES OF CIGS CELLS*.

Meier, J., Bailat, J., Benagli, S., Borrello, D., Vallat-Sauvain, E., Meier, J., Kroll, U., Hoetzel, J., Steinhauser, J., Marmelo, M., Monteduro, G., & Castens, L. (2009). *High efficiency amorphous silicon devices on LP-CVD TCO prepared in industrial Kai-M R&D reactor HIGH-EFFICIENCY AMORPHOUS SILICON DEVICES ON LPCVD-ZNO TCO PREPARED IN INDUSTRIAL KAI TM-M R&D REACTOR*. https://www.researchgate.net/publication/237150668

Moore, J. E., Dongaonkar, S., Chavali, R. V. K., Alam, M. A., & Lundstrom, M. S. (2014a). Correlation of built-in potential and I-V crossover in thin-film solar cells. *IEEE Journal of Photovoltaics*, *4*(4), 1138–1148. https://doi.org/10.1109/JPHOTOV.2014.2316364

Moore, J. E., Dongaonkar, S., Chavali, R. V. K., Alam, M. A., & Lundstrom, M. S. (2014b). Correlation of built-in potential and I-V crossover in thin-film solar cells. *IEEE Journal of Photovoltaics*, *4*(4), 1138–1148. https://doi.org/10.1109/JPHOTOV.2014.2316364

Naghavi, N., Abou-Ras, D., Allsop, N., Barreau, N., Bücheler, S., Ennaoui, A., Fischer, C. H., Guillen, C., Hariskos, D., Herrero, J., Klenk, R., Kushiya, K., Lincot, D., Menner, R., Nakada, T., Platzer-Björkman, C., Spiering, S., Tiwari, A. N., & Törndahl, T. (2010). Buffer layers and transparent conducting oxides for chalcopyrite Cu(In,Ga)(S,Se)2 based thin film photovoltaics: present status and current developments. *Progress in Photovoltaics: Research and Applications*, *18*(6), 411–433. https://doi.org/10.1002/PIP.955

Nakamura, M., Yamaguchi, K., Kimoto, Y., Yasaki, Y., Kato, T., & Sugimoto, H. (2019a). Cd-Free Cu(In,Ga)(Se,S)2 thin-film solar cell with record efficiency of 23.35%. *IEEE Journal of Photovoltaics*, *9*(6), 1863–1867. https://doi.org/10.1109/JPHOTOV.2019.2937218

Nakamura, M., Yamaguchi, K., Kimoto, Y., Yasaki, Y., Kato, T., & Sugimoto, H. (2019b). Cd-Free Cu(In,Ga)(Se,S)2 thin-film solar cell with record efficiency of 23.35%. *IEEE Journal of Photovoltaics*, *9*(6), 1863–1867. https://doi.org/10.1109/JPHOTOV.2019.2937218

Nardone, M., Patikirige, Y., Walkons, C., Bansal, S., M.Friedlmeier, T., E.Kweon, K., B.Varley, J., & Lordi, V. (2018). *2018 IEEE 7th World Conference on Photovoltaic Energy Conversion (WCPEC) (A Joint Conference of 45th IEEE PVSC, 28th PVSEC & 34th EU PVSEC) : 10-15 June 2018.*

Niki, S., Contreras, M., Repins, I., Powalla, M., Kushiya, K., Ishizuka, S., & Matsubara, K. (2010). CIGS absorbers and processes. *Progress in Photovoltaics: Research and Applications*, *18*(6), 453–466. https://doi.org/10.1002/pip.969

Parida, B., Iniyan, S., & Goic, R. (2011). A review of solar photovoltaic technologies. In *Renewable and Sustainable Energy Reviews* (Vol. 15, Issue 3, pp. 1625–1636). https://doi.org/10.1016/j.rser.2010.11.032

Paul, S., Grover, S., L.Repins, I., M.Keyes, B., A.Contreras, M., Ramanathan, K., Noufi, R., Zhao, Z., Liao, F., & V.Li, J. (2018). *Analysis of back contact*.

Peng, J., Lu, L., & Yang, H. (2013). Review on life cycle assessment of energy payback and greenhouse gas emission of solar photovoltaic systems. In *Renewable and Sustainable Energy Reviews* (Vol. 19, pp. 255–274). Elsevier Ltd. https://doi.org/10.1016/j.rser.2012.11.035

Pettersson, J., Platzer-Björkman, C., & Edoff, M. (2009). Temperature-dependent current-voltage and lightsoaking measurements on Cu(In,Ga)Se2 solar cells with ALD-Zn1-xMgxO buffer layers. *Progress in Photovoltaics: Research and Applications*, *17*(7), 460–469. https://doi.org/10.1002/pip.912

PHOTOVOLTAICS REPORT. (2022, December 6). https://www.ise.fraunhofer.de/content/dam/ise/de/documents/publications/studies/Photovoltaics-Report.pdf

Poortmans, J., & Arkhipov, V. (2006). *Thin Film Solar Cells Fabrication, Characterization and Applications Edited by*.

Prokesch, M., Irmscher, K., Rinas, U., Makino, H., & Yao, T. (2002). Net acceptor concentration in ZnSe:Sb grown from vapor phase. In *Journal of Crystal Growth* (Vol. 242).

Rau, U., Braunger, D., Herberholz, R., Schock, H. W., Guillemoles, J. F., Kronik, L., & Cahen, D. (1999). Oxygenation and air-annealing effects

on the electronic properties of Cu(In,Ga)Se2 films and devices. *Journal of Applied Physics*, *86*(1), 497–505. https://doi.org/10.1063/1.370758

Sakurai, K., Yamada, A., Fons, P., Matsubara, K., Kojima, T., Niki, S., Baba, T., Tsuchimochi, N., Kimura, Y., & Nakanishi, H. (2003). Adjusting the sodium diffusion into CuInGaSe2 absorbers by preheating of Mo/SLG substrates. *Journal of Physics and Chemistry of Solids*, *64*(9–10), 1877–1880. https://doi.org/10.1016/S0022-3697(03)00173-2

Salhi, B. (2022). The Photovoltaic Cell Based on CIGS: Principles and Technologies. In *Materials* (Vol. 15, Issue 5). MDPI. https://doi.org/10.3390/ma15051908

Salome, P. M. P., Hultqvist, A., Fjallstrom, V., Edoff, M., Aitken, B. G., Zhang, K., Fuller, K., & Kosik Williams, C. (2014). Incorporation of Na in Cu(In,Ga)Se2 thin-film solar cells: A statistical comparison between Na from soda-lime glass and from a precursor layer of NaF. *IEEE Journal of Photovoltaics*, *4*(6), 1659–1664. https://doi.org/10.1109/JPHOTOV.2014.2357261

Salomé, P. M. P., Rodriguez-Alvarez, H., & Sadewasser, S. (2015). Incorporation of alkali metals in chalcogenide solar cells. In *Solar Energy Materials and Solar Cells* (Vol. 143, pp. 9–20). Elsevier B.V. https://doi.org/10.1016/j.solmat.2015.06.011

Sampaio, P. G. V., & González, M. O. A. (2017). Photovoltaic solar energy: Conceptual framework. In *Renewable and Sustainable Energy Reviews* (Vol. 74, pp. 590–601). Elsevier Ltd. https://doi.org/10.1016/j.rser.2017.02.081

Scully, J. (2021, August 24). *CdTe breakthrough could lead to more efficient solar cells, UK researchers say - PV Tech*. https://www.pv-tech.org/cdte-breakthrough-could-lead-to-more-efficient-solar-cells-uk-researchers-say/

Shin, Y. M., Lee, C. S., Shin, D. H., Kwon, H. S., Park, B. G., & Ahn, B. T. (2015). Surface modification of CIGS film by annealing and its effect on the band structure and photovoltaic properties of CIGS solar cells. *Current Applied Physics*, *15*(1), 18–24. https://doi.org/10.1016/j.cap.2014.09.023

Sozzi, G., Cojocaru-Miredin, O., & Wuerz, R. (2021). A simulation study on the effect of sodium on grain boundary passivation in CIGS thin-film solar cells. *Conference Record of the IEEE Photovoltaic Specialists Conference*, 187–191. https://doi.org/10.1109/PVSC43889.2021.9518887

Sze, S. M., & Lee, M. K. (n.d.). *3RD EDITION Semiconductor Devices Physics and Technology*.

Uppsala Universitet. (2011). *Alternative back contact for CIGS solar cells built on sodium-free substrates WilhelmSöderström*. http://www.teknat.uu.se/student

Venkata Ratan, R. (2019). *'Surface passivation effects of aluminium oxide on ultra-thin CIGS solar cells'*. http://hdl.handle.net/2078.1/172512

Wada, T., Kohara, N., Nishiwaki, S., & Negami, T. (2001). Characterization of the Cu(In,Ga)Se2/Mo interface in CIGS solar cells. *Thin Solid Films*, *387*(1–2), 118–122. https://doi.org/10.1016/S0040-6090(00)01846-0

Wiatros-Motyka, M., Jones, D., Broadbent, H., Fulghum, N., Dizon, R., & Macdonald, P. (n.d.). *Lead authors Analysis contributors*.

Yun, J. H., Kim, K. H., Kim, M. S., Ahn, B. T., Ahn, S. J., Lee, J. C., & Yoon, K. H. (2007). Fabrication of CIGS solar cells with a Na-doped Molayer on a Na-free substrate. *Thin Solid Films*, *515*(15 SPEC. ISS.), 5876–5879. https://doi.org/10.1016/j.tsf.2006.12.156

ANNEXES

ANNEX A – EXPERIMENTAL RESULTS

	Cell	Voc (mV)	Jsc (A/cm2)	Rp (ohm)	Rs(ohm)	FF (%)	Ef (%)
Reference	2	613.33	3.42E-02	9.32E+02	1.54	79.98	15.21
	3	618.84	3.44E-02	9.32E+02	1.62	68.11	15.47
	4	623.04	3.44E-02	8.27E+02	1.81	76.08	15.15
	10	620.29	3.43E-02	9.66E+02	1.59	78.08	15.29
	12	649.33	3.44E-02	7.53E+02	4.76	68.14	12.38
	14	622.63	3.43E-02	8.70E+02	1.90	69.73	14.73
	15	625.41	3.41E-02	6.89E+02	2.02	68.26	14.57
	16	629.28	3.38E-02	9.88E+02	2.11	67.88	14.43
	19	629.49	3.42E-02	9.55E+02	1.92	69.87	15.06
	20	630.43	3.41E-02	8.00E+02	1.78	69.82	15.13
	21	631.15	3.42E-02	1.07E+03	1.85	69.46	14.98
	22	632.29	3.41E-02	9.61E+02	1.93	68.54	14.78
	23	636.53	3.38E-02	9.37E+02	1.96	68.89	14.84
O_2	2	598.29	3.37E-02	5.36E+02	1.72	70.67	14.31
	7	589.98	3.42E-02	1.05E+03	1.95	70.16	14.14
	8	589.34	3.36E-02	1.21E+03	2.24	78.78	13.65
	9	613.33	3.37E-02	9.36E+02	1.50	73.14	14.94
	10	605.54	3.40E-02	9.82E+02	1.56	70.41	14.87
	11	601.23	3.44E-02	9.45E+02	1.51	65.36	14.87
	12	597.98	3.45E-02	9.00E+02	1.65	67.86	14.77
	13	597.34	3.45E-02	9.31E+02	1.69	76.21	14.71
	14	597.75	3.43E-02	1.15E+03	1.77	69.21	14.58
	15	598.87	3.38E-02	9.52E+02	1.86	61.43	14.43
	18	610.28	3.35E-02	1.16E+03	1.50	65.62	14.75
	19	605.15	3.34E-02	1.35E+03	1.64	65.60	14.65
	20	602.46	3.27E-02	9.11E+02	1.65	75.60	14.09
	21	605.05	3.20E-02	8.17E+02	4.06	62.16	12.04
	22	606.06	3.15E-02	9.81E+02	1.81	75.74	13.68
	23	609.59	3.07E-02	1.19E+03	1.99	68.18	13.42
	24	613.27	2.97E-02	1.30E+03	2.94	68.09	12.41
Na free	8	487.53	3.22E-02	9.94E+02	13.52	50.38	7.91
	11	476.34	3.33E-02	6.23E+02	20.94	48.21	7.65
	12	475.98	3.34E-02	6.68E+02	19.96	48.18	7.66
	13	477.76	3.35E-02	6.90E+02	18.38	48.42	7.74
	14	479.75	3.33E-02	7.39E+02	16.55	48.86	7.80
	19	478.98	3.29E-02	5.98E+02	23.92	46.99	7.41
	20	480.17	3.29E-02	6.11E+02	27.06	47.44	7.50
	21	481.39	3.30E-02	6.77E+02	24.62	47.77	7.60
	22	485.47	3.29E-02	6.74E+02	20.57	48.38	7.73
	23	486.82	3.29E-02	6.74E+02	18.43	49.13	7.88
	27	484.19	3.19E-02	5.51E+02	30.71	46.37	7.15
	28	485.49	3.22E-02	3.81E+02	29.34	37.30	5.83
	29	487.13	3.23E-02	5.99E+02	23.94	47.66	7.51
	30	489.84	3.22E-02	6.81E+02	20.72	48.42	7.64
	31	491.25	3.20E-02	7.47E+02	21.93	49.13	7.73

Figure A1 - Numerical results obtained from the JV curve of each cell

Reference				O_2				Na free		
Cell	Ncv (0 Volts)	w (0 nm)		Cell	Ncv (0 Volts)	w (0 nm)		Cell	Ncv (0 Volts)	w (0 nm)
2	7.86E+15	336.02		2	3.76E+15	416.47		8	5.88E+14	1078.52
3	7.88E+15	337.94		7	4.38E+15	418.05		11	1.57E+14	1662.92
10	7.42E+15	346.25		8	5.10E+15	413.83		12	2.20E+14	1845.81
12	7.12E+15	358.24		10	3.29E+15	406.54		13	2.09E+14	1446.18
14	6.47E+15	386.02		11	3.44E+15	407.75		14	2.74E+14	1342.55
15	6.42E+15	395.26		12	3.63E+15	409.46		19	1.34E+14	1702.25
16	5.68E+15	432.09		13	3.50E+15	410.69		20	1.44E+14	1623.86
19	6.52E+15	370.19		15	4.27E+15	420.42		21	1.79E+14	1529.82
21	6.64E+15	396.01		18	4.08E+15	406.49		22	2.54E+14	1387.17
22	6.98E+15	403.38		19	3.84E+15	409.85		23	3.16E+14	1301.64
23	5.83E+15	423.45		20	3.24E+15	420.29		27	1.44E+14	1640.52
				21	2.90E+15	439.31		28	1.66E+14	1569.89
				22	2.82E+15	456.70		29	2.08E+14	1467.54
				23	2.74E+15	484.90		30	2.67E+14	1378.18
				24	3.07E+15	492.43		31	3.38E+14	1288.22

Figure A2 - Numerical results obtained using the derivative method, representing the N_{CV} and width of the depletion region of each of the cells